J. Fluid Mech. (1984), *vol.* 147, *pp.* 397–429
Printed in Great Britain

Mean-flow and turbulent characteristics of free and impinging jet flows

By M. K. LOONEY† AND J. J. WALSH
Chemical Engineering Department, University College Dublin,
Upper Merrion Street, Dublin 2, Ireland

(Received 27 June 1983 and in revised form 15 April 1984)

Numerical solutions are presented of the governing equations for three plane flows: the laminar free jet; the developing turbulent free jet; and the turbulent impinging jet for different ratios h/b of the nozzle height h above the plate to the nozzle width b.

The accuracy of the numerical procedure is demonstrated by comparing the solution of the Navier–Stokes equations for the laminar-flow case with their analytical boundary-layer solution. For turbulent flows these equations are solved after Reynolds averaging. Closure is achieved by a two-equation turbulence model in conjunction with three alternative algebraic expressions for the turbulent stresses. The capabilities of such an approach are illustrated by the extent and consistency of the predictions and the satisfactory agreement of the measurable quantities with the more reliable experimental data in the literature. The limitations of the models employed, evident from their lack of universality, are discussed in the light of their derivation from more complex 'single-point' closures.

Features of the flows studied of interest include: the near-nozzle behaviour of a 'finite' laminar free jet; the potential core and transition regions of a turbulent free jet, along with the fully developed similarity profiles; the enhanced heat-transfer characteristics of impinging jet flows; and the similarity of the developing wall jet after impingement to the standard wall-jet configuration.

1. Introduction

In recent years it has become increasingly viable to tackle turbulent-flow problems in engineering by solving the complete time-averaged Navier–Stokes equations in conjunction with a turbulence closure. This study formed part of a wider task of applying these numerical modelling techniques to fluid-flow problems in chemical engineering. Of particular interest is impingement drying (Looney 1982), a common industrial operation involving the drying of such diverse products as paper, textiles, peat pots and on moving beds by the impingement of hot air issuing from rows of plane nozzles. This paper concentrates on the hydrodynamic predictions of some of the more relevant flows involved in the operation.

The solution of the plane laminar free jet is obtained primarily to examine the accuracy of the numerical method. This is achieved by comparing the developed jet solution with the analytical boundary-layer solution of Schlichting (1933) and Bickley (1939), which has been confirmed experimentally by Andrade (1939) for jet Reynolds numbers Re_j up to 30. In addition, the predictions also illustrate the

† Present address: Mechanical Engineering Department, Imperial College of Science and Technology, Exhibition Road, London SW7 2BX.

near-nozzle flow resulting from real 'finite' inlet conditions. The plane turbulent free jet is studied primarily to provide the accurate specification of the upstream boundary conditions for the impinging-jet case, i.e. the potential core and undeveloped flow regions are of interest. Previous studies have been confined to the fully developed flow region. The solution also provides an opportunity of testing the performance of the most suitable contemporary turbulence models in predicting this well-documented flow, while confirming the earlier findings of turbulence-model developers regarding the fully developed flow predictions. Finally the plane turbulent impinging jet is solved for a wide range of h/b ratios and Reynolds numbers in order to study their effect on the important augmented heat-transfer characteristics near the stagnation point.

The time-averaged continuity and Navier–Stokes equations are solved for steady turbulent flow of an incompressible fluid. Based on conclusions drawn from a study of previous numerical work (see §3 and Looney 1982), the turbulence models considered are confined to those involving two additional partial differential equations. Of these, the standard k-ϵ turbulence model of Jones & Launder (1972) is selected owing to its success in handling a wide variety of free and wall-bounded flows with and without recirculation (Launder & Spalding 1974). In addition modifications to the k-ϵ model in the form of Rodi's (1972) suggestions for modelling both strong and weak shear flows and Ljuboja & Rodi's (1979) algebraic stress model for wall-bounded flows are selected owing to their previous success in predicting a self-similar free jet and wall jet respectively. The use of the word 'prediction' in the context of the turbulence-model closures selected and the turbulent free-jet solution requires some clarification, as this flow was included in the group of test cases from which the various turbulence model constants have been optimized (see §4.1). However, bearing in mind that it was the fully developed free jet that was involved, that the only axial variation considered was its spreading rate and the fact that 24 flows were involved in the case of the standard k-ϵ model (Launder *et al.* 1972) and five flows in the case of Rodi's (1972) model, it appears justified.

The finite-volume method employed in the solution of the equations is in many respects conventional: the elliptic equations being formulated in their primitive-variable form, on a non-uniform Cartesian mesh and solved for iteratively. The procedure, termed CHAMPION 2/E/FIX (Pun & Spalding 1976), was selected owing to the partially parabolic nature of the flows studied, being a 'line-by-line' iterative procedure solving the equations sequentially along each 'staggered' grid-line before proceeding downstream. It handles the coupling of the continuity and momentum equations by solving for pressure via the SIMPLE (semi-implicit method for pressure linked equations) algorithm of Patankar & Spalding (1972). Details of the efficiency of the numerical procedure in handling the flows involved are provided, along with some preliminary results, by Looney & Walsh (1982).

2. Experimental work

2.1. *The free jet*

The plane turbulent free jet has been investigated experimentally at various levels as illustrated in table 1. Included are details of the nozzle width b and aspect ratio s, the jet Reynolds number $Re_j = \rho U_0 b/\mu$ ($U_0 \equiv$ inlet velocity) and the distance downstream over which measurements were taken, along with a list of the mean-flow and turbulence quantities measured.

Much of the experimental data is in conflict in certain areas, owing to both the

Experimenter	Nozzle dimensions	Range x/b	Re_j	Mean-flow quantities measured	Turbulence quantities measured
Forthmann (1934)	$b = 30$ mm $s = 12.7$	25	7.0×10^4	U	—
Miller & Comings (1957)	$b = 12.7$ mm $s = 40$	40	2.0×10^4	U, p	$\overline{u^2}$
Van der Hegge Zijnen (1958)	$b = 5$ and 10 mm $s = 20$	40	1.33×10^4	U, V	$\overline{u^2}, \overline{v^2}, \overline{uv}$
Bradbury (1965)	$b = 9.53$ mm $s = 48$ $U_\infty = 0.16\, U_0$	70	3.0×10^4	U, V, p	$\overline{u^2}, \overline{v^2}, \overline{w^2}, \overline{uv}, l, \lambda_s$, k-balance
Heskestad (1965)	$b = 12.7$ mm $s = 132$	160	4.7×10^3– 3.7×10^4	U	$\overline{u^2}, \overline{v^2}, \overline{w^2}, \overline{uv}, \overline{u_i u_j u_k}$, k and k_{CL} balance
Patel (1970)	$b = 7$ mm $s = 114$	152	3.5×10^4	U	$\overline{u^2}, \overline{v^2}, \overline{w^2}, \overline{uv}$, k and $\overline{uv}$ balance
Mih & Hoopes (1972)	$b = 1.73$ mm $s = 59$	140–300	1.77×10^4– 3.14×10^4	U	$\overline{u^2}, \overline{v^2}, \overline{uv}, l, \lambda_s$
Robins (1973)	$b = 3.2$–19 mm $s = 128$–21	100	7.0×10^3– 7.5×10^4	U, V, p	$\overline{u^2}, \overline{v^2}, \overline{w^2}, \overline{uv}$, l, k and $\overline{uv}$ balance
Gutmark & Wygnanski (1976)	$b = 13$ mm $s = 38.5$	120	3.0×10^4	U, V	$\overline{u^2}, \overline{v^2}, \overline{w^2}, \overline{uv}$, $\epsilon, \lambda_s, \overline{u_i u_j u_k}$, k and k_{CL} balance
Hussain & Clark (1977)	$b = 31.8$ mm $s = 44$	40	3.26×10^4 and 8.14×10^4	U, p	$\overline{u^2}$
Antonia, Satyaprakash & Hussain (1980)	$b = 31.8$ mm $s = 44$	160	2.04×10^4 and 4.28×10^4	U_{CL}	ϵ, l, λ_s

$U, V \equiv$ mean velocities, $u, v, w \equiv$ fluctuating velocities, $p \equiv$ static pressure, $k \equiv$ turbulent kinetic energy, $\epsilon \equiv$ turbulent-energy dissipation rate, $l =$ mixing length, $\overline{u_i^2} \equiv$ normal stresses, $\overline{uv} \equiv$ shear stress, $\lambda_s \equiv$ microscales, ϕ-balance $\equiv$ lateral variation of individual terms of ϕ-equation, ϕ_{CL} balance $\equiv$ axial variation of individual terms of ϕ_{CL} equation.

TABLE 1. Experimental data for plane turbulent free jet

variety of inlet and boundary conditions employed, many of which are inadequately reported, and the level of experimental error inherent in hot-wire anemometry, by which the majority of the experimental data is obtained. The former problem is well illustrated by the findings of Kotsovinos (1976), who correlated existing mean-velocity data and reported a nonlinear growth rate, i.e. a spreading rate ($\mathrm{d}\delta/\mathrm{d}x$) which varied from 0.0913 at $x < 30b$ to 0.14 at $x > 300b$ ($\delta \equiv$ half-width $\equiv y$ at $U = \frac{1}{2}U_{CL}$, where $U_{CL} \equiv$ centreline jet velocity). However, Bradshaw (1977) showed that the increased spreading rate may be due to the fall in the mean velocity and turbulence intensity of the jet to the same order of magnitude as that of the fluctuating draughts (of sufficiently long wavelength for the jet to be translated sideways) in the room caused by the recirculation of the fluid. He showed that the reported increase in spreading rate corresponds to a background turbulence level of 0.5 % of the inlet velocity. The latter problem was quantified by Robins (1973), who estimated an experimental error of ± 8 % in his fluctuating-velocity measurements and demonstrated that much larger errors can occur in measurements near the edge of the jet ($y > 1.5\delta$), where turbulence intensities are high.

Rodi (1975), in his review of experimental data for free jets, assessed Bradbury's (1965), Heskestad's (1965), Patel's (1970), Gutmark & Wygnanski's (1976) and

Robins' (1973) data. Based on a comparison of measured and calculated (from mean-velocity measurements) shear stress $\overline{uv}$, he found, not surprisingly, that Bradbury's data is the most consistent, since the existence of a slow parallel stream ($U_\infty = 0.16U_0$) reduced the turbulence intensities at the edge of the jet. He also quotes a downstream spreading-rate figure of 0.11, similar to that found by Heskestad. However, considering the findings of Bradshaw (1977) mentioned above and that Newman (1967), in his review of experiments up to 1965, recommends a figure of $0.104 \pm 2\%$ which is in agreement with the later findings of Robins (1973), 0.103, Gutmark & Wygnanski (1976), 0.1, and Hussain & Clark (1977), 0.1, this figure would appear to be too high.

2.2. *The impinging jet*

Those workers who have carried out flow and heat-transfer measurements in plane turbulent impinging jets are listed in table 2. Included are details of the nozzle width, the nozzle aspect ratio, the jet Reynolds number, the height h of the nozzle above a flat plate, and the distance along the plate over which measurements were taken, along with a list of the flow and heat-transfer quantities measured.

Few complete studies of mean-flow and turbulence characteristics have been undertaken. Russell & Hatton's (1972) and Gutmark, Wolfshtein & Wygnanski's (1978) data represent the only available fluctuating-velocity measurements. However, the former employed a very low nozzle aspect (length/width) ratio of 6 and reported a high initial turbulence intensity due to inadequate plenum-chamber design; the latter study was confined to centreline measurements at a nozzle height of one hundred slot widths. In addition, Beltaos & Rajaratnam's (1973) mean-flow data and Gardon & Akfirat's (1965, 1966) local heat-transfer-coefficient data represent the only extensive measurements for different h/b ratios undertaken.

3. Previous numerical modelling work

3.1. *The free jet*

Owing to their high turbulence intensities, the prediction of turbulent free jets has been employed as a crucial test case in the development of many turbulence models. However, in almost all cases the boundary-layer equations, which neglect the normal-stress terms, were solved in stream-function–vorticity form using iterative techniques (e.g. Patankar & Spalding 1967) which march forward from in most cases arbitrary initial conditions until profiles reach similarity. Thus only downstream spreading rate and U, k, $\overline{uv}$ and k-balance (see (6)) similarity profiles were reported.

Rodi & Spalding (1970), employing a version of Rotta's (1969) k-kl turbulence model, predicted a downstream spreading rate of 0.108 and turbulence quantities which were underpredicted by up to 5% compared with Bradbury's experimental data. Later, Rodi (1972) repeated the calculations using an empirical function for the turbulent viscosity constant (see (8)) and optimized all constants to predict flows with either strong or weak strain. This resulted in a spreading rate of 0.114 and overprediction of the k and $\overline{uv}$ profiles in the outer part of the jet by up to 10%. Launder *et al.* (1972) confirmed that Rodi's (1972) suggestions, applied to the k-ϵ model, improved the prediction of the linear relationship $(1 - U_{CL}/U_0)^{-2}$ versus x/b for a plane free jet in a moving stream. Launder & Morse (1977) found that the Reynolds-stress closure of Launder, Reece & Rodi (1975) gave too high a prediction (0.123) for the spreading rate of the plane jet.

Experimenter	Nozzle dimensions	Re_j	$\frac{h}{b}$	Width $\frac{y}{h}$	Flow and heat-transfer quantities measured
Schauer & Eustis (1963)	—	4.3×10^4	40	0.3	U, p_w, V_m,
Kumada & Mabuchi (1970)	$b = 5$ and 10 mm $s = 60$ and 30	7×10^3–2.8×10^4	2–40	10–0.5	V_m, p_w
Russell & Hatton (1972)	$b = 25.4$ mm $s = 6$	1.25×10^5	31.5	0.3175	$U, \overline{u^2}, \overline{v^2}, \overline{w^2}, \overline{uv}, l, \mu_t$
Beltaos & Rajaratnam (1973)	$b = 2.24$ mm $s = 65$	5.27×10^3–9.4×10^3	14.04–67.5	7.5	U, V, p, τ_w
Bower, Kotansky & Hoffman (1977)	$b = 38.1$ mm $s = 40$	1.3×10^5 and 3.8×10^5	1–4	4–1	U_{CL}, k_{CL}, p
Gutmark, Wolfshtein & Wygnanski (1978)	$b = 13$ mm $s = 38.5$	3×10^4	100	0	$U_{CL}, \overline{u^2_{CL}}, \overline{v^2_{CL}}, \overline{w^2_{CL}}, \epsilon_{CL}, \lambda_{sCL}, \overline{u_i^2}_{CL}$ and k_{CL} balance τ_w
Baines & Keffer (1980)	$b = 1.9$ mm $s = 263$	7×10^3	2–20	7.5–0.75	τ_w
Gardon & Akfirat (1966)	$b = 1.59$–6.35 mm $s = 96$–24	450–5×10^4	0.33–80	10–0.75	Nu, h_1, h_{av}
Gardon & Akfirat (1965)	$b = 3.2$ mm $s = 48$	1.1×10^4	2–32	10–0.75	p_w, h_1
Van Heiningen, Mujumdar & Douglas (1977)	$b = 6.2$ and 14.1 mm	1.37×10^4–4.91×10^4	2.6 and 6.0	8.5	Nu
Hardisty (1977)	$b = 3.0$ mm	3×10^3–1×10^4	2–16	7.5–1.0	h_1

TABLE 2. Experimental data for plane turbulent impinging jet. $p_w \equiv$ wall static pressure, $\tau_w \equiv$ wall shear stress, V_m = maximum velocity parallel to the plate, $h_1 \equiv$ local wall heat-transfer coefficient, $h_{av} \equiv$ average h_1, $Nu \equiv$ local Nusselt number $= h_1 b/k_f$, $k_f \equiv$ thermal conductivity of the fluid.

3.2. *The impinging jet*

The most detailed study on plane impinging jets was completed by Wolfshtein (1967). He employed Prandtl's (1945) one-equation model and later a form of Kolmogorov's (1942) k-f^2 model (Wolfshtein 1969), and solved the equations in stream-function–vorticity form for the impingement region only. His inlet conditions included similarity stream-function and vorticity profiles and a constant turbulent kinetic-energy level. He found that, compared with Schauer & Eustis' (1963) experimental data, his predictions for wall shear stress, wall pressure and mean velocity V_m were too low, and his predicted Nu-profile along the plate had an incorrect minimum appearing at the stagnation point. He attributed the faults to both an inaccurate turbulent viscosity law and his near-wall boundary conditions. Other workers, including Russell & Hatton (1972), Bower & Kotansky (1976) and Bower *et al.* (1977), repeated aspects of Wolfshtein's work employing similar boundary conditions. Van Heiningen *et al.* (1977) carried out some 'preliminary' numerical predictions with the standard k-ϵ model, solving the stream-function–vorticity equations at $Re_j = 22750$ and $h/b = 8$. They found their stagnation Nusselt-number prediction to be too low compared with Gardon & Akfirat's (1966) measurements, attributing the failure to their 'wall functions' (see (13) and (14)).

Recently Agarwal & Bower (1982), in their study of VTOL aircraft design, included normal jet impingement in their calculations, employing the low-Reynolds-number k-ϵ turbulence model of Jones & Launder (1973), i.e. allowing them to dispense with wall functions. They also confined their solution field to the impingement region, using empirical inlet profiles, and reported excellent agreement for their ground-plane static-pressure results with Schauer & Eustis' (1963) and Gardon & Akfirat's (1965) data. Their remaining calculations included both incompressible and compressible flow cases at $h/b = 2$ with the undersurface of the fuselage as upper boundary condition. They reported good agreement with their static-pressure and mean-velocity measurements, but predicted a large overshoot in turbulent kinetic energy along the jet centreline near the ground plane compared with their measurements.

4. Methodology

4.1. *The equations solved*

For steady laminar isothermal plane flow of an incompressible Newtonian fluid of density ρ and viscosity μ, the continuity and Navier–Stokes equations become

$$\frac{\partial U_j}{\partial x_j} = 0, \tag{1}$$

$$\rho U_j \frac{\partial U_i}{\partial x_j} = -\frac{\partial p}{\partial x_i} + \frac{\partial}{\partial x_j}\left\{\mu\left(\frac{\partial U_i}{\partial x_j} + \frac{\partial U_j}{\partial x_i}\right)\right\}, \tag{2}$$

where $i, j = 1, 2$ and summation over repeated indices applies; $U_i \equiv$ instantaneous velocity, $p =$ static pressure.

For turbulent flow the complete equations are Reynolds-averaged, resulting in additional stresses, which, from the turbulent-viscosity law, become

$$-\rho\overline{u_i u_j} = \mu_t\left(\frac{\partial U_i}{\partial x_j} + \frac{\partial U_j}{\partial x_i}\right) - \tfrac{2}{3}\delta_{ij}\rho k, \tag{3}$$

where $U_i \equiv$ mean velocity, $u_i \equiv$ fluctuating velocity, $k = \frac{1}{2}\overline{u_i u_i}$, overbar $\equiv$ ensemble average, $\mu_t \equiv$ turbulent viscosity (to be defined by turbulence model), $\delta_{ij} \equiv$ Kronecker

delta. Thus the final equations are identical with (1) and (2) except for the transformations $\mu \rightarrow \mu_{\text{eff}} = \mu + \mu_t$ and $p \rightarrow p_s + \frac{2}{3}\rho k$.

The stagnation-enthalpy ($\tilde{H}$) equation, required for the impinging-jet case, includes a turbulent-flux term $-\partial(\rho u_j \overline{\tilde{H}'})/\partial x_j$, which, to be consistent with the turbulent-viscosity assumption, is modelled assuming a turbulent thermal diffusivity:

$$-\overline{u_j \tilde{H}'} = \lambda_t \frac{\partial \tilde{H}}{\partial x_j}, \tag{4}$$

where $\tilde{H} = \int_{T_0}^{T} c_p \, dT + \frac{1}{2} U_j U_j + k$, $T \equiv$ temperature, $c_p \equiv$ specific heat, $\tilde{H}' \equiv$ fluctuating stagnation enthalpy $= H' + \frac{1}{2} u_j u_j$, $\lambda_t \equiv$ turbulent thermal diffusivity $= \nu_t/\sigma_t$, $\nu_t = \mu_t/\rho$, $\sigma_t \equiv$ turbulent Prandtl number $= 0.9$ for near-wall flows. Therefore the stagnation-enthalpy equation can be written as

$$\rho U_j \frac{\partial \tilde{H}}{\partial x_j} = \frac{\partial}{\partial x_j}\left\{\left(\frac{\mu}{\sigma_1} + \frac{\mu_t}{\sigma_t}\right)\frac{\partial \tilde{H}}{\partial x_j}\right\} + \frac{\partial}{\partial x_j}\left\{\left(\mu - \frac{\mu}{\sigma_1}\right)\left(\frac{1}{2}\frac{\partial U_i U_i}{\partial x_j} + \frac{\partial k}{\partial x_j}\right)\right\}, \tag{5}$$

where $\sigma_1 \equiv$ Prandtl number $= c_p \mu / k_f$ (if it is of order unity the last term on the right-hand side becomes negligible).

The turbulent viscosity is assumed to be a function of the turbulent kinetic energy k and the turbulent-energy dissipation rate ϵ, which are obtained from their own transport equations (Jones & Launder 1972):

$$\rho U_j \frac{\partial k}{\partial x_j} = \frac{\partial}{\partial x_j}\left\{\left(\mu + \frac{\mu_t}{\sigma_k}\right)\frac{\partial k}{\partial x_j}\right\} + \rho P - \rho \epsilon, \tag{6}$$

$$\rho U_j \frac{\partial \epsilon}{\partial x_j} = \frac{\partial}{\partial x_j}\left\{\left(\mu + \frac{\mu_t}{\sigma_\epsilon}\right)\frac{\partial \epsilon}{\partial x_j}\right\} + \rho C_1 \frac{\epsilon P}{k} - C_2 \frac{\rho \epsilon^2}{k}, \tag{7}$$

where

$$P = V_t\left(\frac{\partial U_i}{\partial x_j} + \frac{\partial U_j}{\partial x_i}\right)\frac{\partial U_i}{\partial x_j}, \quad \epsilon = \nu \overline{\frac{\partial u_i}{\partial x_j}\frac{\partial u_i}{\partial x_j}},$$

$$C_1, C_2, \sigma_k, \sigma_\epsilon = \text{constants}.$$

The ϵ-equation is preferred to the kl-equation employed by Rodi (1972) on the evidence of Launder & Spalding (1974). They have shown the difference between the equations lies in the diffusion term, which, though unimportant in free shear layers where l does not vary laterally, becomes important near a wall where l is proportional to the distance from the wall. If both equations are reduced for near-wall flow to expressions for σ, the Prandtl number for turbulent transport, then only in the case of the ϵ-equation is this expression applicable, when standard coefficient values are inserted, to the spread of the different entities (kl and ϵ) at locations far from walls.

If the modelled form of the Reynolds-stress equations (Launder *et al.* 1975) are reduced by assuming the convection and diffusion terms to be proportional to those of the k-equation multiplied by the ratio $\overline{u_i u_j}/k$, in accordance with a suggestion of Rodi (1972), they can be transformed to become

$$-\rho(\overline{u_i u_j} - \tfrac{2}{3}\delta_{ij} k) = \tfrac{2}{3}(1-\alpha)\left[\frac{C_{s1} - 1 + \alpha P/\epsilon}{(C_{s1} - 1 + P/\epsilon)^2}\right]\frac{\rho k^2}{\epsilon}\left(\frac{\partial U_i}{\partial x_j} + \frac{\partial U_j}{\partial x_i}\right), \tag{8}$$

where α and C_{s1} are constants associated with the mean-strain and turbulence interaction effects of the pressure–strain correlation respectively, and are set at 0.6 (Crow 1968) and 2.486 as recommended by Hanjalic & Launder (1972). The term in the square brackets reduces to 0.09 when the production-to-dissipation P/ϵ ratio is set at unity, and corresponds closely to the optimized empirical function for the

turbulent viscosity constant employed by Rodi (1972) in his predictions of free turbulent boundary layers. Hence (6)–(8) will be termed Rodi's (1972) algebraic stress model. In deriving (8), further details of which are given by Rodi (1980), the surface integral (and hence wall effects) in the pressure–strain correlation is neglected and turbulent stresses are assumed to be influential in thin shear layers only, which places some limitations on the application of all two-equation models to such complex flows as impinging jets. On the other hand, the stress-redistribution part of the pressure–strain correlation, found by Gutmark *et al.*(1978) to be important in the stagnation region of an impinging jet, is included. An expression for the turbulent viscosity can now be deduced from (8), which, if $P/\epsilon = 1$, reduces to

$$\mu_t = C_D \rho k^2/\epsilon, \tag{9}$$

where $C_D = 0.09$ for the standard k-ϵ model.

The remaining constants appearing in (6) and (7) are subject to the constraints

$$1.83 < C_2 < 2.0, \tag{10}$$

from experimental data for the decay of turbulence behind a grid in the absence of mean velocity gradients, and

$$1.83 - \frac{0.533}{\sigma_\epsilon} < C_1 < 2.0 - \frac{0.533}{\sigma_\epsilon}, \tag{11}$$

from near-wall turbulence data. With the additional constraint that both the k and ϵ Prandtl numbers are the order of unity, Launder *et al.* (1972) optimized the five constants for the standard k-ϵ model for a wide range of free shear flows to those values given in table 3.

If the surface integral appearing in the modelled pressure–strain correlation term of the Reynolds-stress equations is included before their reduction to algebraic form (in order to obtain the measured damping of the level of fluctuating velocity normal to a surface and the enhancement of the level parallel to the main flow), a turbulent-viscosity expression results of the form (Ljuboja & Rodi 1979)

$$\mu_t = \frac{F_D G_1 G_2 \rho k^2}{\epsilon}, \tag{12}$$

where

$$F_D = \frac{2(1-\alpha)(C_{s1}-1+\alpha P/\epsilon)}{3C_{s1}(C_{s1}-1+P/\epsilon)},$$

$$G_1 = \frac{1+1.5\alpha C_2' f/(1-\alpha)}{1+1.5C_1' f/C_{s1}},$$

$$G_2 = \frac{1-2\alpha C_2' Pf/(C_{s1}\epsilon-\epsilon+\alpha P)}{1+2C_1' f/(C_{s1}-1+P/\epsilon)},$$

$$f = \min\left[1.0, \frac{k^{\frac{3}{2}}}{C_w \delta_{w1} \epsilon}\right], \quad \delta_{w1} \equiv \text{distance from wall},$$

$$C_{s1} = 2.2, \quad \alpha = 0.55 \quad \text{(Launder 1975)},$$

$$C_1' = 0.75, \quad C_2' = 0.45$$

(which were adjusted to achieve the correct ratios of $\overline{u^2}$, $\overline{v^2}$ and $\overline{uv}$ to k close to the wall),

$$C_w = 4.4 \quad \text{so that } f \text{ becomes unity next to the wall.}$$

C_D	σ_k	C_2	σ_ϵ	C_1
0.09	1.0	1.92	1.3	1.43

TABLE 3. Standard k-ϵ model constants

In practice, when $P/\epsilon = 1$, F_D reduces to 0.1085, which is rectified by replacing F_D with the constant C_D. Thus (9), (8) and (12), together with table 3, represent three separate turbulence models of increasing complexity. Their validity in representing the mean-flow and turbulence characteristics of free and impinging jets will be tested here.

To overcome the requirement of fine grids adjacent to walls in turbulent flow, 'wall functions' are introduced to calculate quantities at grid points that are placed well outside the viscous sublayer. They take the form of expressions for the wall shear stress from which average production and dissipation of k across the near-wall 'cell' may be estimated. For the impinging-jet case, Launder & Spalding's (1974) modified log-law wall function is employed, which plausibly accounts for the diffusion of turbulence energy from the free stream and is given by

$$\tau_w = \frac{KC_D^{\frac{1}{4}}\rho V k^{\frac{1}{2}}}{\ln\left(EC_D^{\frac{1}{4}}\rho\delta_{w1}k^{\frac{1}{2}}/\mu\right)}, \tag{13}$$

where $V \equiv$ mean velocity parallel to the wall at δ_{w1}; $K = 0.4$ and $E = 9.0$ from universal log-law velocity profile.

Finally the rate of heat transport from a wall, q_w, is calculated from τ_w using the classical non-dimensionalized temperature profile:

$$q_w = \frac{\tau_w}{V}\frac{H_w - \tilde{H}}{\max\{\sigma_1, \sigma_t[1+(\tau_w/\rho V^2)^{\frac{1}{2}}]P_f\}}, \tag{14}$$

where

$$P_f = \frac{\frac{1}{4}\pi}{\sin\frac{1}{4}\pi}\left(\frac{A}{K}\right)^{\frac{1}{4}}\left[\frac{\sigma_1}{\sigma_t}-1\right]\left(\frac{\sigma_t}{\sigma_1}\right)^{\frac{1}{4}},$$

from the analysis of experimental data by Jayatilleke (1969); $A =$ a constant depending on the roughness of the wall ($A = 26.0$ for a smooth wall).

4.2. *Method of solution*

The finite-volume solution procedure is described in detail by Pun & Spalding (1976). Briefly, the solution domain is discretized into a non-uniform rectangular mesh. The finite-difference equations for each variable are derived by approximate integration of the parent differential equations over each control 'volume', ensuring the preservation of their conservation properties. The variable 'nodes' are arranged so that the velocities are located midway between the pressures which drive them (see figure 1). The resultant finite-difference equations connect each nodal value of variable ϕ to its four nearest neighbours by linear algebraic relations. Thus for node P

$$A_P\phi_P = \sum_i A_i\phi_i + S_{\phi,P}, \tag{15}$$

where $A \equiv$ coefficient representing convection and diffusion, $S_{\phi,P} \equiv$ integrated source, $A_P = \Sigma_i A_i$, $\Sigma_i \equiv$ summation over node P's four neighbours. They are solved iteratively along successive lines in the main flow direction (if one exists) using the

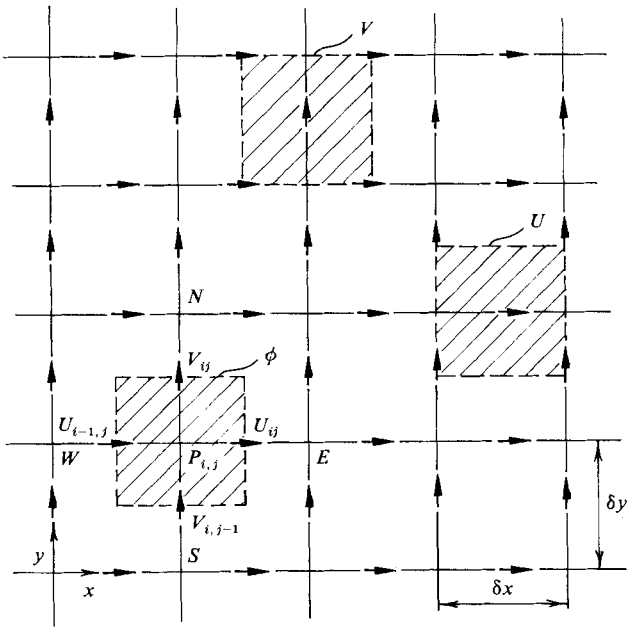

FIGURE 1. A staggered rectangular mesh illustrating the ϕ (i.e. p, k and ϵ), U and V control 'volumes'.

Thomas tridiagonal-matrix algorithm. A pressure-perturbation equation can be derived, from a combination of the discretized continuity and momentum equations, in the general form of (15). Its solution yields updated pressures which drive the velocities in the direction of satisfying continuity.

The non-uniform rectangular meshes allow for grid refinement where gradients are large. A hybrid differencing scheme combining the advantages of both upwind and central differencing is employed to ensure stability at all Péclet numbers (i.e. $\rho U_i \delta x_i/\mu$) and to reduce the effects of numerical diffusion, which are greatest when streamlines travel at 45° with respect to the coordinate directions.

5. Results and discussion of numerical predictions

5.1. *Laminar free jet*

An isothermal two-dimensional submerged laminar free jet is studied. For the test case, air at 15 °C ($\rho = 1.226$ kg/m^3 and $\mu = 1.75 \times 10^{-5}$ N s/m^2) is issuing from a nozzle ($b = 6$ mm) at 50 mm/s and $Re_j = 20$. A solution field of length $L = 102.5b$ and width $W = 53.3b$ is covered by a 34×30 node mesh to achieve a grid-independent solution. Boundary conditions are

$$U = V = 0 \quad \text{on the top wall,}$$

$$\frac{\partial U}{\partial y} = V = 0 \quad \text{on the axis of symmetry,}$$

$$\frac{\partial U}{\partial y} = \frac{\partial V}{\partial y} = 0 \quad \text{on the free boundary,}$$

$$U = U_{CL} f\left(\frac{y}{\delta}\right), \quad \frac{\partial V}{\partial x} = 0 \quad \text{downstream,}$$

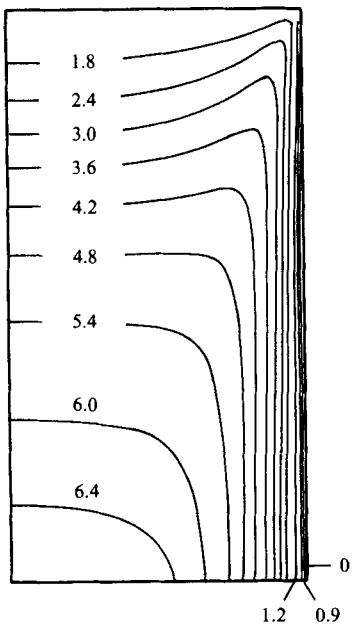

FIGURE 2. Streamlines (units of cm^2/s) representing half the laminar free-jet flow field.

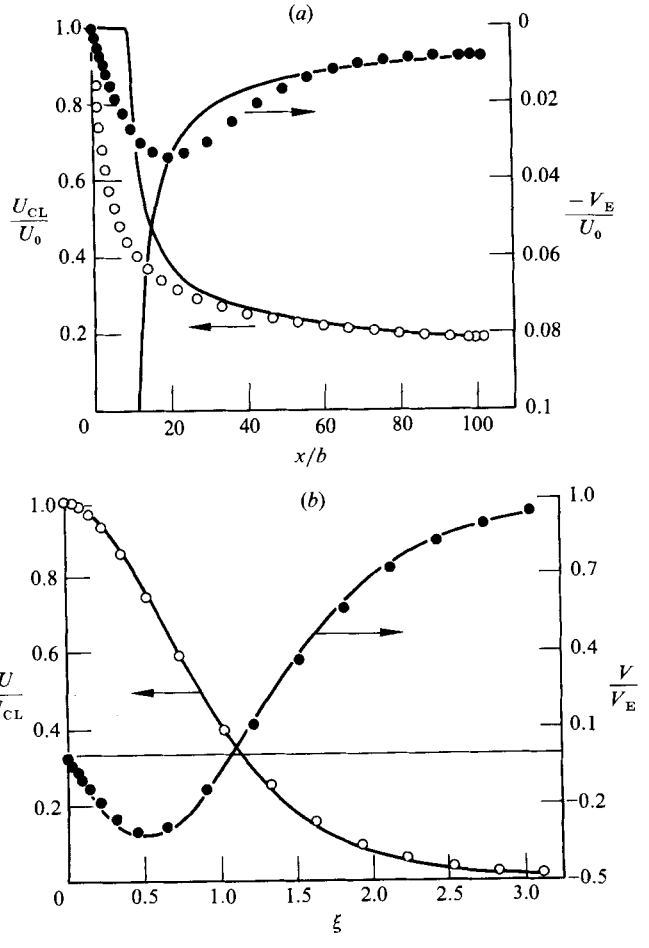

FIGURE 3(*a*, *b*). For caption see p. 408.

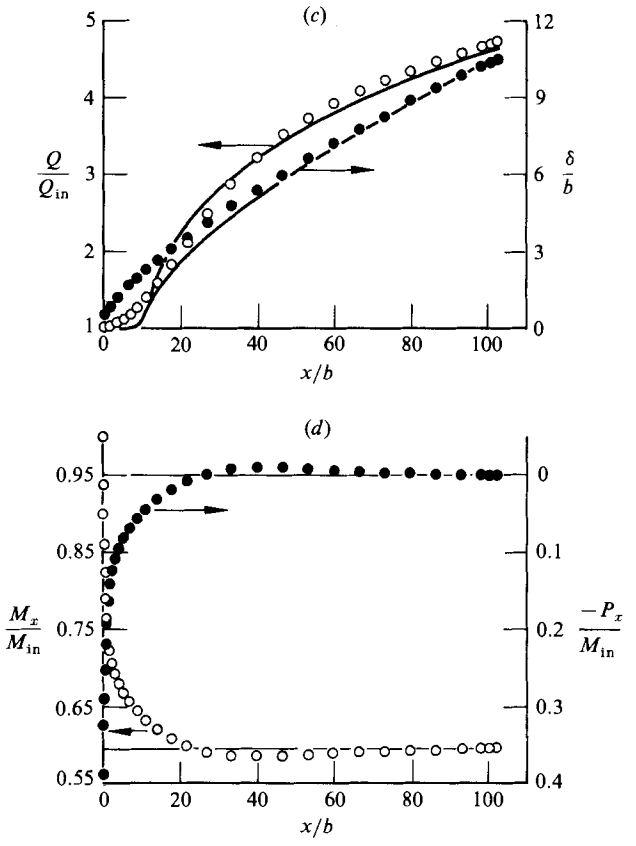

FIGURE 3. Comparison between the computational (○, ●) and the analytical (——) solution for the laminar free jet: (*a*) axial distribution of centreline velocity U_{CL} and entrainment velocity V_E; (*b*) U and V similarity profiles; (*c*) spreading rate: Q/Q_{in} and δ/b versus x/b; (*d*) momentum and pressure fluxes.

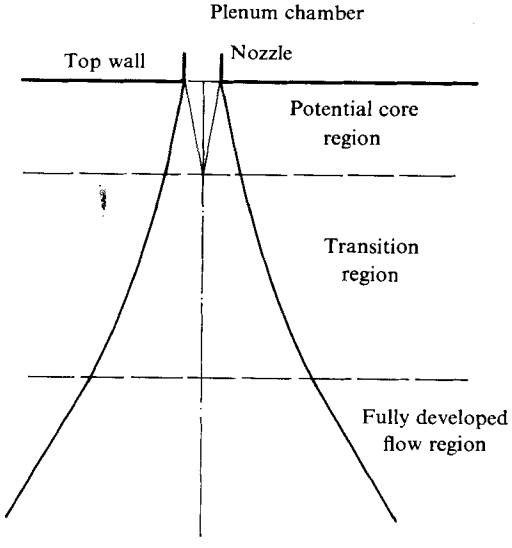

FIGURE 4. The turbulent free jet.

where f is defined by extrapolation from the previous grid line assuming similarity, i.e. U/U_{CL} versus y/δ, $U_{\mathrm{CL}} \propto x^{-\frac{1}{3}}$, $\delta \propto x^{\frac{2}{3}}$. The calculated streamlines for the flow are shown in figure 2.

Figures 3(*a–d*) demonstrate the accuracy of the solution procedure by comparing the predictions with the analytical boundary-layer solution of Schlichting (1933) and Bickley (1939). The latter is obtained by selecting a suitable value for the lateral momentum M_x and the position of the origin, i.e. a correction to the distance x from the nozzle, to allow for comparison with solutions for a finite inlet condition, i.e. $b \neq 0$ and $U \neq \infty$. From figure 3(*d*) M_x approaches a constant value of $0.594 M_{\mathrm{in}}$, and from figure 3(*a*) the origin x_0 is at $9.6b$, corresponding to matching values of U_{CL} at $93.3b$. Hence the analytical solution is calculated from

$$
\begin{aligned}
U &= 0.4543\left(\frac{M_x^2}{\rho\mu x}\right)^{\frac{1}{3}}(1-\tanh\xi),\\
\xi &= 0.2752\left(\frac{M_x}{\mu x}\right)^{\frac{1}{3}}\frac{y}{x^{\frac{2}{3}}},\\
V &= 0.5503\left(\frac{M_x\mu}{\rho^2x^2}\right)^{\frac{1}{3}}[2\xi(1-\tanh^2\xi)-\tanh\xi],\\
Q &= 3.302\rho\left(\frac{M_x\mu x}{\rho^2}\right)^{\frac{1}{3}},\\
\delta &= 3.203\left(\frac{\mu^2}{\rho M_x}\right)^{\frac{1}{3}}x^{\frac{2}{3}},
\end{aligned}
\tag{16}
$$

where $M_x = \rho\int_{-\infty}^{+\infty} U^2\,\mathrm{d}y$ and $Q \equiv$ mass flow rate.

Agreement between the two solutions is very good, considering their differing inlet conditions. Figure 3(*d*) places this difference in perspective. Whereas the boundary-layer solution assumes an ambient pressure field throughout the flow field, and hence constant momentum M_x, the numerical solution of a 'real' problem indicates a small negative pressure field existing directly beneath the nozzle, resulting in enhanced entrainment (see figure 2) and a sharp fall in the momentum until it levels out at about $25b$ before rising slightly, accompanied by a positive pressure field ($P_x = \int_{-\infty}^{+\infty} p\,\mathrm{d}y$). Both level off after $80b$, where similarity is established conclusively and identical U- and V-profiles result, as shown in figure 3(*b*).

The overall rate of spread $\Delta\delta/\Delta x$ at this Re_{j} is shown in figure 3(*c*) to be 0.103. Therefore the solution represents a good test case to illustrate any numerical diffusion errors that might distort the results of the turbulent free-jet solution, which will have a similar spreading rate and hence average angular streamline variation with coordinate axes. Figure 3 demonstrates that these are minor. To confirm this result, grid-independence tests for both turbulent flows are also carried out.

5.2. *Turbulent free jet*

An isothermal two-dimensional submerged turbulent free jet is studied (see figure 4). For the test case, air at 15 °C is issuing from a nozzle (b = 13 mm) at 35 m/s, 0.2 % turbulence intensity and $Re_{\mathrm{j}} = 3\times10^4$. A solution field of length $L = 44b$ and width $W = 22b$ is covered by a 40×36 node mesh to achieve a 'grid-independent' solution, the variation in centreline mean and turbulent quantities in moving from a 40×36

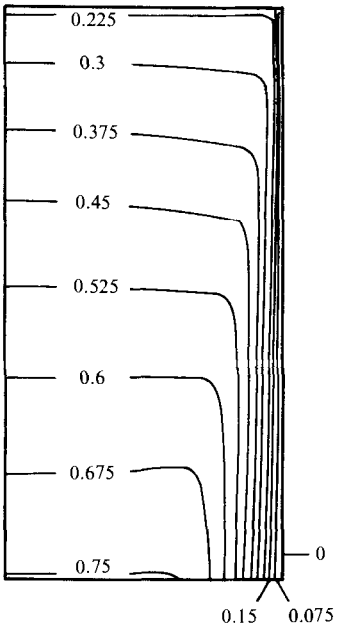

FIGURE 5. Streamlines (units of m^2/s) representing half the turbulent free-jet flow field.

mesh to a 50^2 mesh solution being less than 1% and 2% respectively. Boundary conditions are

$$U = V = k = \epsilon = 0 \quad \text{on the top wall,}$$

$$V = \frac{\partial U}{\partial y} = \frac{\partial k}{\partial y} = \frac{\partial \epsilon}{\partial y} = 0 \quad \text{on the axis of symmetry,}$$

$$\frac{\partial V}{\partial y} = U = k = \epsilon = 0 \quad \text{on the free boundary,}$$

$$\frac{\partial k}{\partial x} = \frac{\partial \epsilon}{\partial x} = 0, \quad U = U_{\mathrm{CL}} f\left(\frac{y}{\delta}\right), \quad V = U_{\mathrm{CL}} g\left(\frac{y}{\delta}\right) \quad \text{downstream,}$$

where f and g are defined by extrapolation from the previous grid line, assuming similarity, i.e. U/U_{CL} versus y/δ, V/U_{Cl} versus y/δ, $U_{\mathrm{CL}} \propto x^{-\frac{1}{2}}$, $\delta \propto x$. The calculated streamlines for the flow are shown in figure 5.

Figures 6(*a–l*) compare the computational results found by employing the standard k-ϵ model (i.e. (9) and table 3) and Rodi's (1972) algebraic stress model (i.e. (8)) with the extensive experimental data listed in table 1. Mean-flow results are represented by the axial distributions of the centreline velocity (*a*), the half-width (*d*) and the centreline static pressure (*h*), the U and V velocity components similarity profiles (*b*) and (*c*), the static pressure profile (*i*) and the lateral distribution of the four terms in the U-momentum equation normalized by $\rho U_{\mathrm{CL}}^2/\delta$ (*k*). While turbulent characteristics are provided by the axial distribution of the centreline turbulent-kinetic-energy (*e*), the k (*f*), shear-stress (*g*) and a normal-stress, $\overline{v^2}$ (*j*) similarity profiles and the lateral distribution of the four terms of the k-equation normalized by $\rho U_{\mathrm{CL}}^3/\delta$ and including the kinetic-energy dissipation-rate profile (*l*). As pointed out earlier, turbulence measurements in the outer part of a jet in still air are not reliable. Hence turbulence-model performance will be based on comparisons within $y < 1.6\delta$, even though all figures include both computational results and measurements, when available, as far out as 2.4δ for completeness.

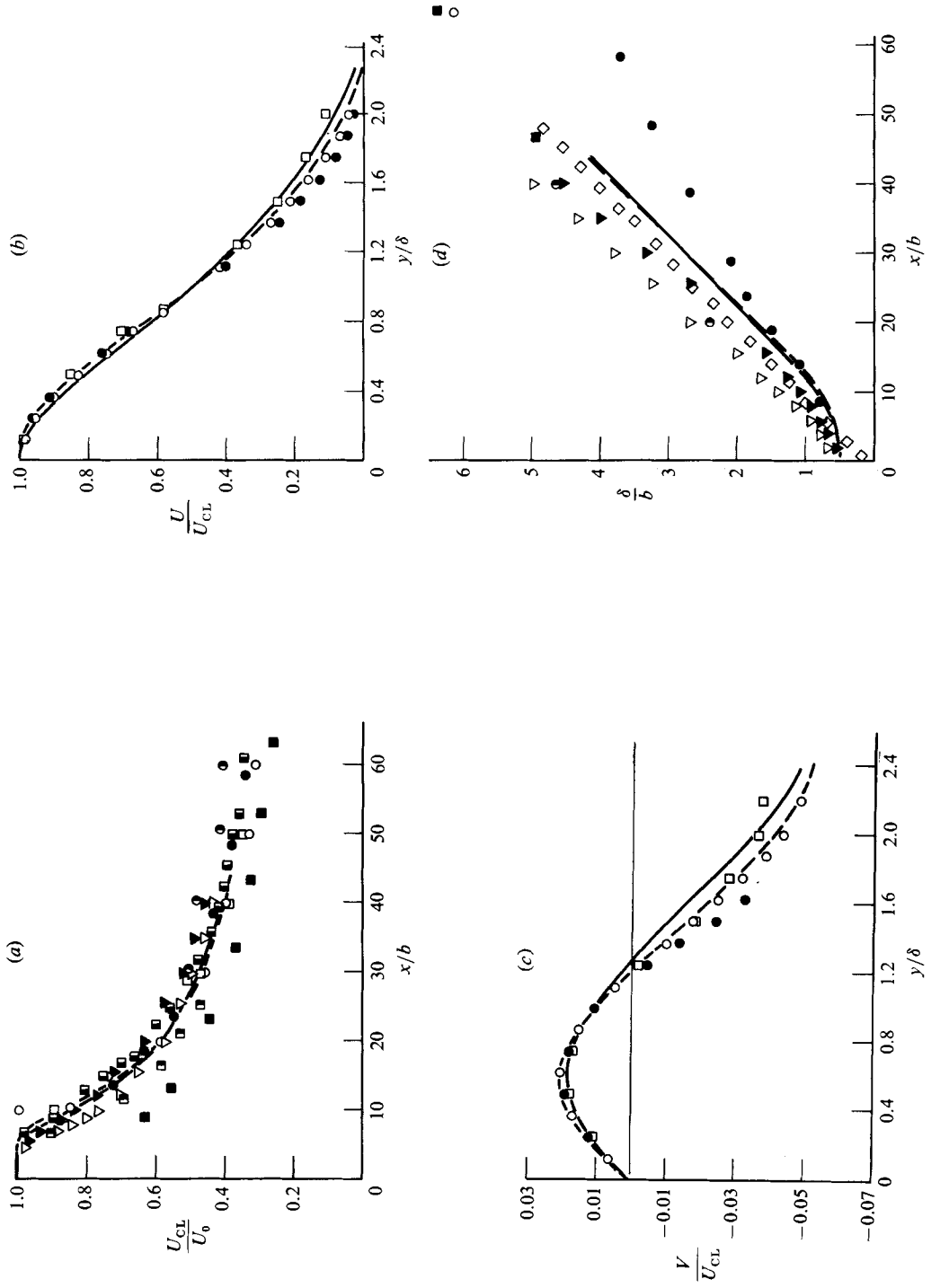

FIGURE 6(*a*, *b*, *c*, *d*). For caption see p. 414.

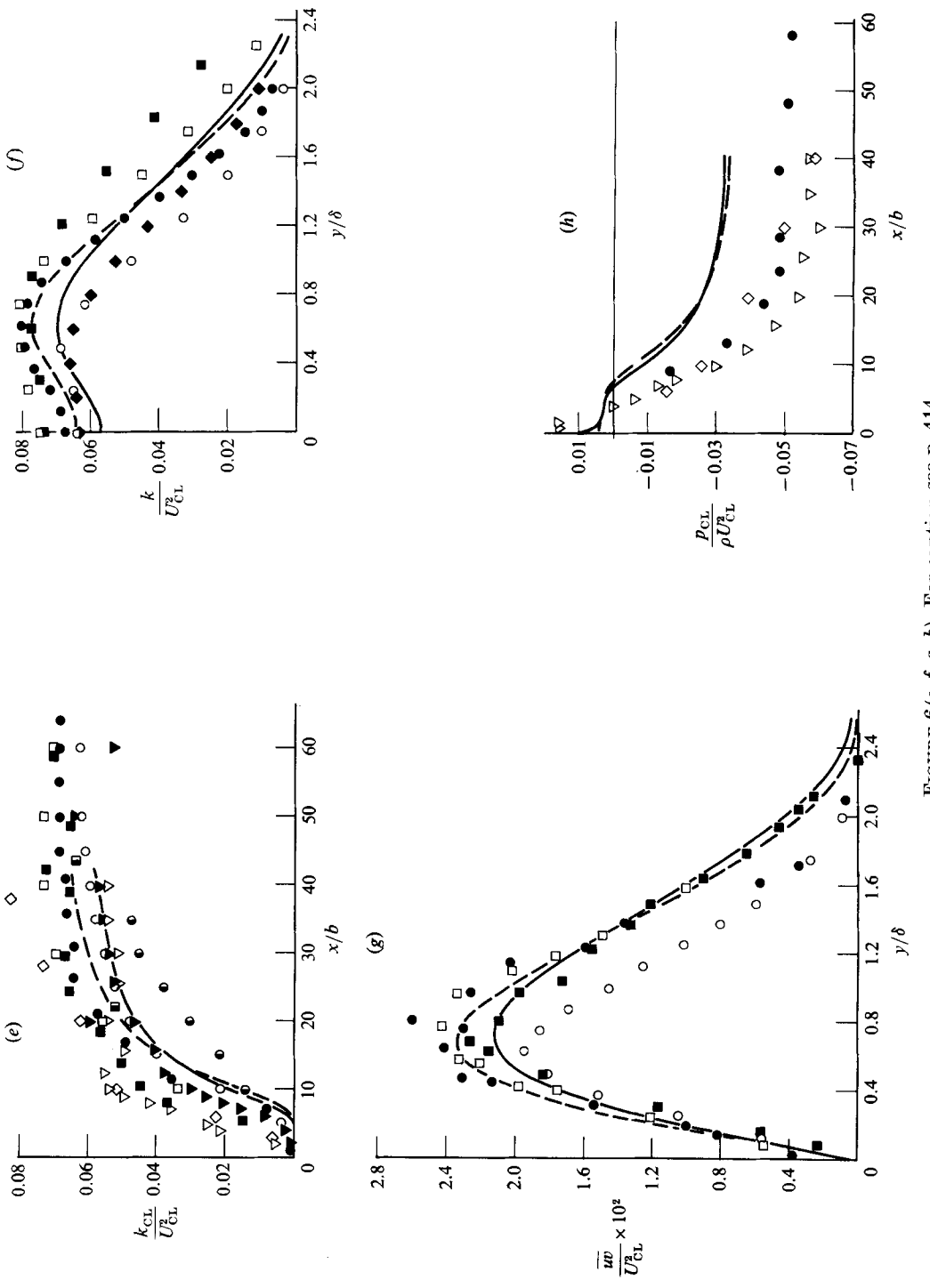

FIGURE 6 (*e*, *f*, *g*, *h*). For caption see p. 414.

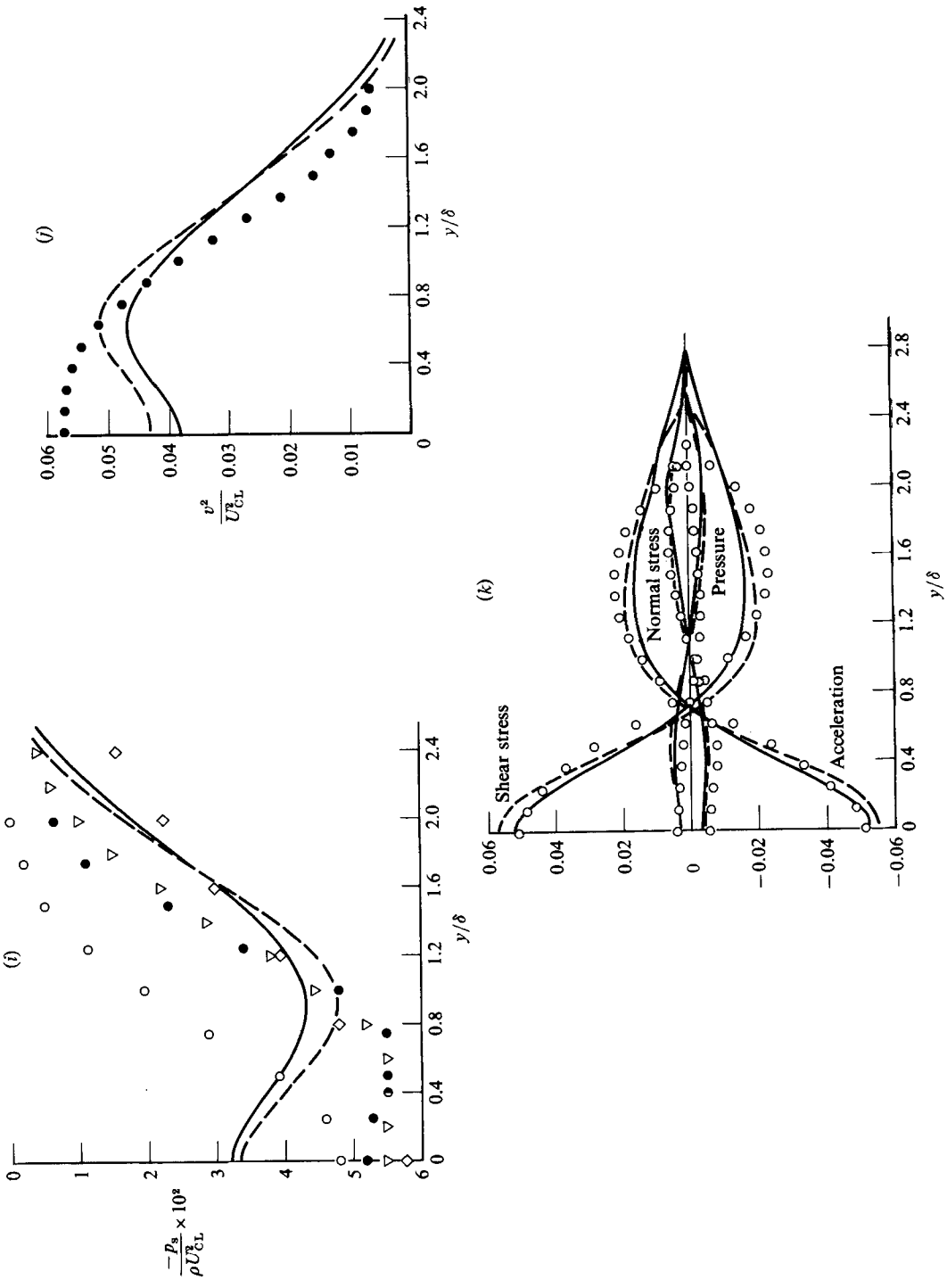

FIGURE 6(*i*, *j*, *k*). For caption see p. 414.

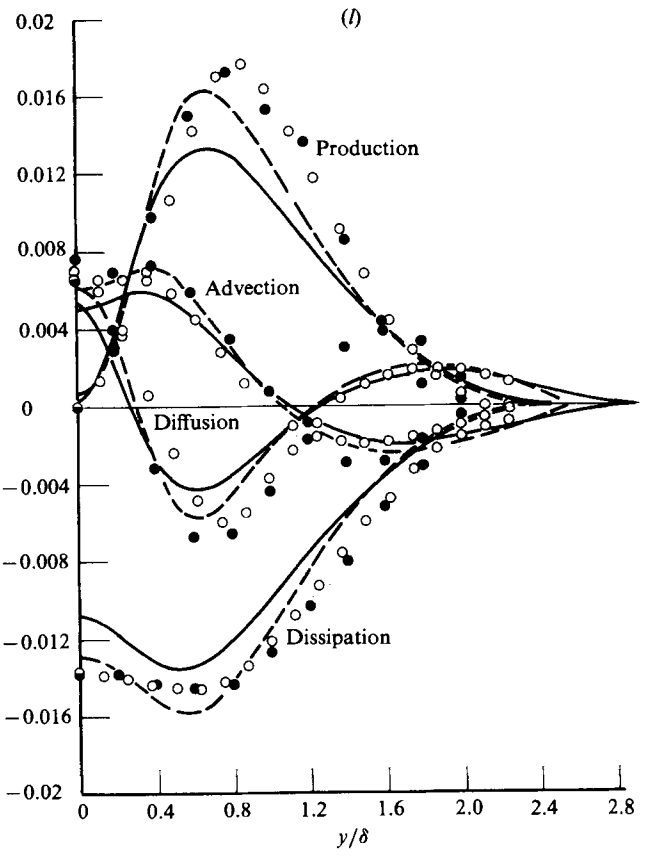

FIGURE 6. Comparison between the numerical solution employing the k-ϵ model (——) and Rodi's (1972) algebraic stress model (– – –) and the experimental data of Bradbury (●), Robins (○), Gutmark & Wygnanski (□), Heskestad (■), Miller & Comings (◇), Van der Hegge Zijnen (◐), Antonia *et al.* (◑), Patel (◆), Forthmann (◨), Mih & Hoopes (◧), and Hussain & Clark for low Re_j (▽) and high Re_j (▼): (*a*) axial distribution of U_{CL}; (*b*) U similarity profile; (*c*) V similarity profile; (*d*) spreading rate: δ/b versus x/b; (*e*) axial distribution of k_{CL}; (*f*) k similarity profile; (*g*) $\overline{uv}$ similarity profile; (*h*) axial distribution of p_{CL}; (*i*) static-pressure profile; (*j*) $\overline{v^2}$ similarity profile; (*k*) U-momentum balance; (*l*) k-equation balance.

The experimental data for the centreline velocity exhibits a great deal of scatter. Even so, agreement between predictions and experiment appears reasonable, considering that Heskestad's (1965), Forthmann's (1934) and Hussain & Clark's (1977) data are all low initially owing to the presence of a smaller potential core ($< 6b$), evident in their k_{CL} distributions also, caused, in the first and third cases at any rate, by inadequate plenum-chamber design. In addition, Bradbury's (1965) data is high downstream owing to the effect of his external stream, and Robins' (1973) data, which indicate a long potential core, have been indirectly calculated from his turbulence measurements. However, Robins' did report a $\mathrm{d}(U_0^2/U_{CL}^2)/\mathrm{d}(x/b)$ value of 0.18, which compares favourably with approximately 0.173 for Rodi's model predictions as opposed to 0.16 for the standard k-ϵ model's results. In addition, the former model's predictions agree better with Gutmark & Wygnanski's (1976) data.

The U and V similarity-profile predictions correspond to a downstream position of $39.45b$, which is consistent with Robins' criteria for self-preservation: $U_{CL}x/\nu > 4 \times 10^5$. They agree well with the experimental data, of which only three

sets are shown for clarity, and Rodi's model predictions appear almost exact. Differing inlet and boundary conditions are again reflected in the experimental data for the half-width. Bradbury's data indicate a spreading rate $\mathrm{d}\delta/\mathrm{d}x$ that is much lower than predictions due to the external stream, and Hussain & Clark's data is affected by the small potential core but implies a spreading rate of 0.1, similar to predictions, i.e. 0.1 from Rodi's model and 0.097 from the standard k-ϵ model. This result is supported by the data of Miller & Comings (1957) (0.1) and the findings of Newman (1967) and others as mentioned earlier (see §2.1). However, it is in marked contrast with the results of Rodi (1972) of 0.108 and 0.114 from his standard and modified k-kl models. The energy-dissipation equation, the more simplified algebraic expression for C_{D} and the inclusion of the normal-stress $\overline{u^2}-\overline{v^2}$ terms in the U-momentum equation perform better in this case.

The scatter exhibited by the k_{CL} data makes it difficult to assess the performance of the two models. This is a result of the differing inlet conditions, illustrated by the scatter in Hussain & Clark's data sets, and the fact that all but Robins' and Gutmark & Wygnanski's data are inferred from $\overline{u^2_{\mathrm{CL}}}/U^2_{\mathrm{CL}}$ and $\overline{u_i^2}$ profile measurements. Yet the two accurate sets of measurements represent good bounding values for the figure. Considering that similarity has not quite been reached, i.e. constant $k_{\mathrm{CL}}/U^2_{\mathrm{CL}}$, in the case of the predictions, it is reasonable to assume that Rodi's model predictions and the bulk of the experimental data will approach each other further downstream (where the inferred data are more reliable) and thus they are preferred. Indeed, this is further borne out by the k and $\overline{uv}$ similarity profiles, where Rodi's model predictions appear slightly lower than the fully developed profiles of Bradbury (which is at $70b$ downstream) and Gutmark & Wygnanski (at $120b$), whose data are considered the more reliable, Robins having pointed out the inconsistency of his $\overline{uv}$-profile with his mean-velocity measurements beyond 0.5δ. Both profiles have maximum values at approximately 0.75δ from the axis, where the velocity gradient $\partial U/\partial y$ and hence $\overline{uv}$ and the production term P are greatest.

Agreement between predictions and experiment for centreline static pressure p_{CL} is poor, particularly downstream. However, this is not the case, once Robins' data is excluded, for the region beyond 0.8δ of the static-pressure profile. Indeed, it is the subsequent rise in p_{s} close to the centreline which results in the poor p_{CL} agreement. This discrepancy between predictions and experiment close to the centreline may be attributed to the fact that the predicted curves are obtained by subtracting $\frac{2}{3}\rho k$ rather than the more correct $\frac{1}{2}(\overline{v^2}+\overline{w^2})$ from the pressure values obtained from the solution of the momentum equations; i.e. isotropic flow is assumed, which is only true when the turbulence is reduced to the smallest scales where dissipation by molecular viscous action occurs (Kolmogorov 1942). Comparison of the $\overline{v^2}$ measurements of Bradbury and the predicted normal-stress profile, i.e. $\frac{2}{3}k$, bears this out, the predicted profile being too low close to the centreline. Indeed a comparison of the two plots of normal stress and static pressure emphasizes this further, and verifies the reduction of the V-momentum equation for fully developed flow by boundary-layer approximations to

$$\frac{p_{\mathrm{s}}}{\rho U^2_{\mathrm{CL}}} = -\frac{\overline{v^2}}{U^2_{\mathrm{CL}}}. \tag{17}$$

However, as $\overline{v^2}$ is not explicitly required in either the momentum (where p rather than p_{s} is included) or the turbulence-model equations, the discrepancy evident in the p_{s} and $\overline{v^2}$ comparisons is unimportant with regard to overall turbulence-model performance.

FIGURE 7. Effective-viscosity contours from employing: (*a*) the standard k-ϵ model (0.003–0.03 N s/m^2); (*b*) Rodi's (1972) algebraic curve stress model (0.003–0.042 N s/m^2).

In the lateral distribution of the four terms of the U-momentum equation, $\partial^2_3 k/\partial x$ has been subtracted from the predicted $\partial p/\partial x$ term and added to the normal-stress term to be consistent with Robins' measurements. Agreement between predictions and experiment is good within 1.6δ. The boundary-layer nature of the flow is clearly indicated by the dominating acceleration and turbulent shear-stress terms, with the former changing sign as V and hence $V\partial U/\partial y$ does so, and the zero values corresponding to the maximum in the $\overline{uv}$-curve.

Finally a comparison of the predicted lateral distributions of the four terms of the k-equation with Robins' and Bradbury's data indicates good agreement, with a clear preference for results from Rodi's algebraic stress model. However, it must be pointed out that, in the case of the experimental data shown, the diffusion term is calculated from a balance of the four terms and then scaled, along with the dissipation term, to achieve zero overall diffusion. This is a result of the difficulty in obtaining accurate dissipation-rate measurements and is evident from Heskestad's and Gutmark & Wygnanski's data, which is unscaled and not shown for clarity but indicates much lower (by 30%) dissipation and hence other terms. The distributions do show the importance of the advection terms over the initial jet half-width and hence the inadequacy of 'zero-equation' turbulence models where production and dissipation are assumed to balance.

Only in the case of the effective viscosity $\mu + \mu_t$ do the variable field contours vary in shape in going from the standard k-ϵ model to Rodi's algebraic stress model (see figures 7 (*a*, *b*): the fluctuations in the outer boundary are caused by the exaggeration, as $\mu_t \propto k^2/\epsilon$, of much smaller ones in the k- and ϵ-values at the edge of the jet as they

fall to zero). The effect of the rising value of C_D for Rodi's model is dramatic (see (8) as $P/\epsilon < 1$). The contours depart from the familiar saddle shape and show a sharp rise next to the centreline. Since this alteration to μ_{eff} has little effect on the shear- and normal-stress terms of the U-momentum equation (see figure 6*j*) or the diffusion term of the k-equation (see figure 6*k*), it must therefore affect the gradients of u, k and ϵ. In fact, it reduces them close to the centreline, and results, as we have shown, in improved predictions, especially in the case of the U- and V-profiles. Thus the unorthodox shape of the μ_{eff} contours for the 'experimentally verified' algebraic stress model point, in the authors' opinion, to the shortcomings of the turbulent-viscosity law, i.e. (3), and the need for its replacement by adequate stress-equation alternatives.

Returning to the experimental verification, it would appear that overall the algebraic stress model of Rodi (1972) provides detailed consistent predictions well within the range of the experimental error reported. The only unsatisfactory comparison involves the dissipation-rate profile, which highlights the discrepancies in existing experimental data. Methods of improving these measurements of what is essentially the turbulence lengthscale must be found before further refinement of the equation can be undertaken. For it is this equation which most workers regard as the weakest link in both the two-equation and stress-equation turbulence models.

5.3. *Turbulent impinging jet*

An isothermal two-dimensional submerged turbulent free jet impinging on a heated flat plate placed at right angles to the centreline is studied for differing values of Re_j and h/b. A partially or fully developed free jet, depending on h/b, is employed as the inlet condition at approximately $0.55h$ (corresponding to 12.2 times the local jet half-width δ) above the plate, with all the quantities specified from the solution of the free-jet problem. The solution field, which extends to approximately $0.55h$ from the centreline to allow the wall jet to develop sufficiently for a similarity velocity-profile side-boundary condition to be applied, is illustrated in figure 8. It is covered by a 35×34 node mesh to achieve 'grid independent' solutions, the variation in centreline and maximum wall-jet quantities in moving from the 35×34 mesh to a 45^2 mesh solution for a typical test case being less than 3 % and 2 % respectively. Boundary conditions are

$$U = V = k = \epsilon = \tilde{H} = 0 \quad \text{on the upper free boundary,}$$

outside the free-jet solution field,

$$V = \frac{\partial U}{\partial y} = \frac{\partial \tilde{H}}{\partial y} = \frac{\partial k}{\partial y} = \frac{\partial \epsilon}{\partial y} = 0 \quad \text{on the axis of symmetry,}$$

$$U = V = k = \frac{\partial \epsilon}{\partial x} = 0, \quad \tilde{H} = H_w \quad \text{at} \quad T_w = 30\ ^\circ\text{C} \quad \text{on the heated plate,}$$

$$\left.\begin{aligned} &\frac{\partial U}{\partial y} = \frac{\partial k}{\partial y} = \frac{\partial \epsilon}{\partial y} = \frac{\partial \tilde{H}}{\partial y} = 0, \\ &\frac{\partial V}{\partial y} = 0 \quad (V < 0), \\ &V = V_m f\left(\frac{x_1}{\delta_1}\right) \quad (V > 0) \end{aligned}\right\} \quad \text{on the side boundary,}$$

where f is defined by extrapolation from the previous grid line, assuming similarity, i.e. V/V_m versus x_1/δ_1, $-V_m \propto y^{-\frac{1}{2}}$, $\delta_1 \propto y$ ($x_1 \equiv$ distance above the plate $= h - x$,

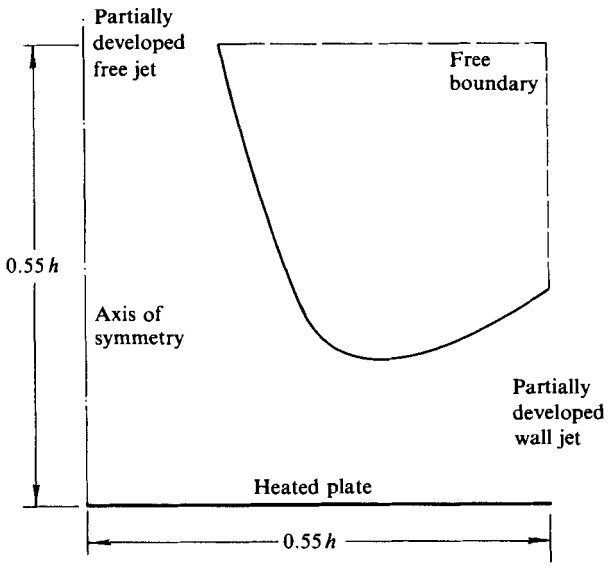

FIGURE 8. The impinging-jet solution field.

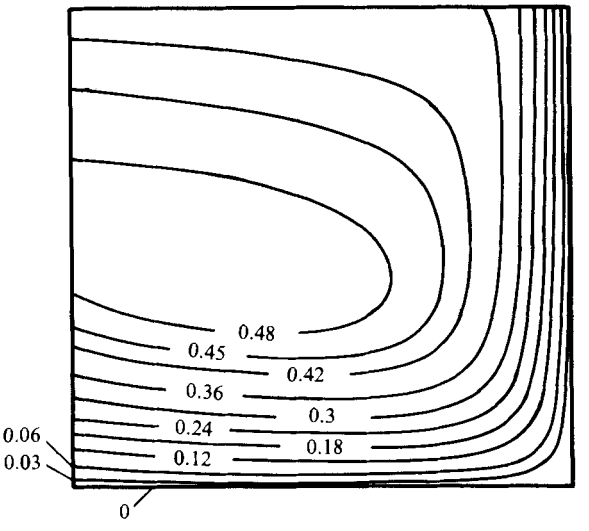

FIGURE 9. Streamlines (units of m^2/s) representing half the turbulent impinging-jet flow field.

$\delta_1 = x_1$ at $V = \frac{1}{2}V_m$). The wall functions are imposed on the solution by setting the coefficient A in (15) referring to the wall node to zero in the approximate momentum and stagnation-enthalpy equations and including the terms $-\tau_w a$ and $q_w a$ respectively on the right-hand side ($a \equiv$ cell-face area), with τ_w and q_w calculated from (13) and (14). The production term of the k-equation is replaced by $\tau_w |\partial V/\partial x|$, and ϵ is calculated directly from k assuming a lengthscale of $0.4\delta_{w1}$.

The calculated streamlines for the flow where $Re_j = 3 \times 10^4$, $b = 13$ mm and $h/b = 20$ are shown in figure 9. They are computed by employing the standard k-ϵ model. The reasons for this turbulence-model choice are illustrated in figure 10, which presents for the three models discussed in §4.1 the axial distribution of U_{CL} and

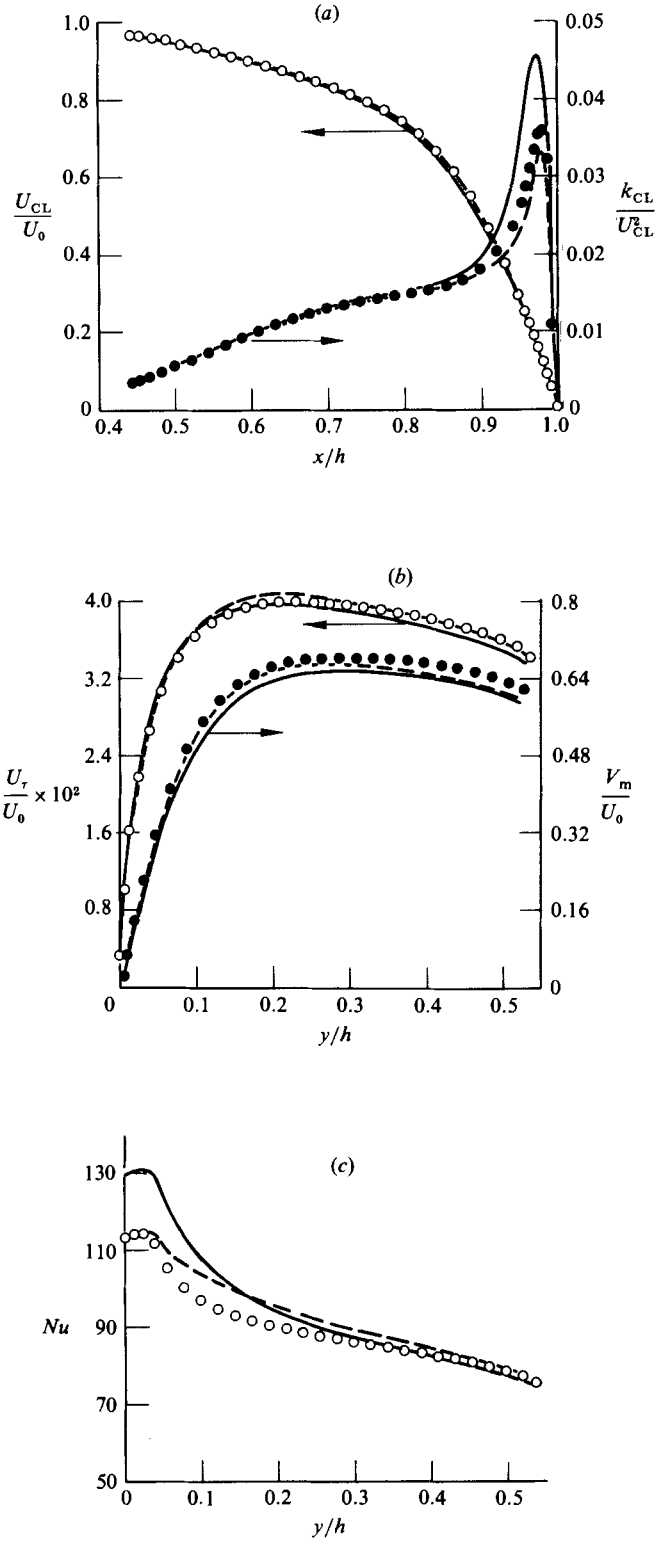

FIGURE 10(*a*, *b*, *c*). For caption see p. 420.

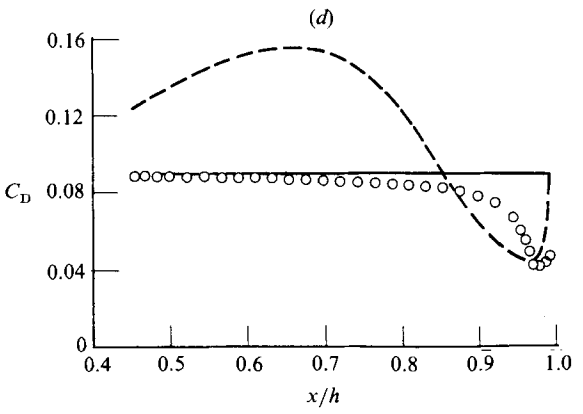

FIGURE 10. Turbulence-model comparison (——, k-ϵ model; – – –, Rodi's model; ○, ● Ljuboja & Rodi's model) for the impinging-jet case: (*a*) axial distribution of U_{CL} and k_{CL}; (*b*) distribution of τ_w and V_m along the plate; (*c*) Nusselt-number profile along the plate; (*d*) centreline values C_D.

k_{CL} (*a*), the variation of τ_w and V_m along the plate (*b*), the local Nusselt-number profile (*c*) and the axial variation of C_D along the centreline (*d*). The main effect of the algebraic stress models is to lower the peak in k_{CL} near the stagnation point. This, along with only small variations in the mean-flow variables near the stagnation point (as they are strongly dominated by non-viscous phenomena), combine to lower Nusselt-number levels near the stagnation point and thereby produce Nu-profiles that differ markedly from experiment (see figure 13). The cause of these differences between the standard and algebraic stress models is the reduction in C_D to approximately 0.04 near the stagnation point. This is due in Rodi's (1972) model to a P/ϵ ratio rising to greater than 2 near the stagnation point, and in Ljuboja & Rodi's (1979) model to a rise in the factor f in (12) from zero to unity as the wall is approached.

The results for the two algebraic stress models are not inconsistent with expectations. For the former has been applied successfully to flows where $P/\epsilon < 1$ only (viz high C_D values, where $P/\epsilon < 1$, in the free-jet solution of figure 10*d*), and the latter has been applied to wall jets only where P/ϵ is close to unity. Thus, owing to the success of the standard k-ϵ model, further modifications such as streamline curvature corrections to either the turbulent-stress approximations (3) or the ϵ-equation have neither been described nor implemented. In addition, discounting its effect on computational resources, extension of the work to Reynolds-stress modelling, in order to achieve a measure of universality for the two turbulent flows considered, would appear fruitless from earlier work on the free jet by Launder & Morse (1977) among others. However, it would have the advantage of predicting correctly the experimentally observed differing positions of zero shear stress and maximum velocity in the wall-jet profiles (see Alcaraz, Charnay & Mathieu 1977). This feature is discussed in detail by Mathieu (1971). It cannot be simulated correctly by a turbulent-viscosity model, which will always predict the velocity maximum to lie too close to the wall. The discrepancy is considered minor in this impinging flow though, and of no practical importance.

Figures 11 (*a–i*) compare the predictions for a wide range of flow variables, employing the standard k-ϵ model, for three test cases: $Re_j = 4.2 \times 10^4$, $h/b = 15$; $Re_j = 3.0 \times 10^4$, $h/b = 20$; and $Re_j = 2.2 \times 10^4$, $h/b = 43$; with the available experimental data listed in table 2. The flow variables include distributions of U_{CL} (*a*),

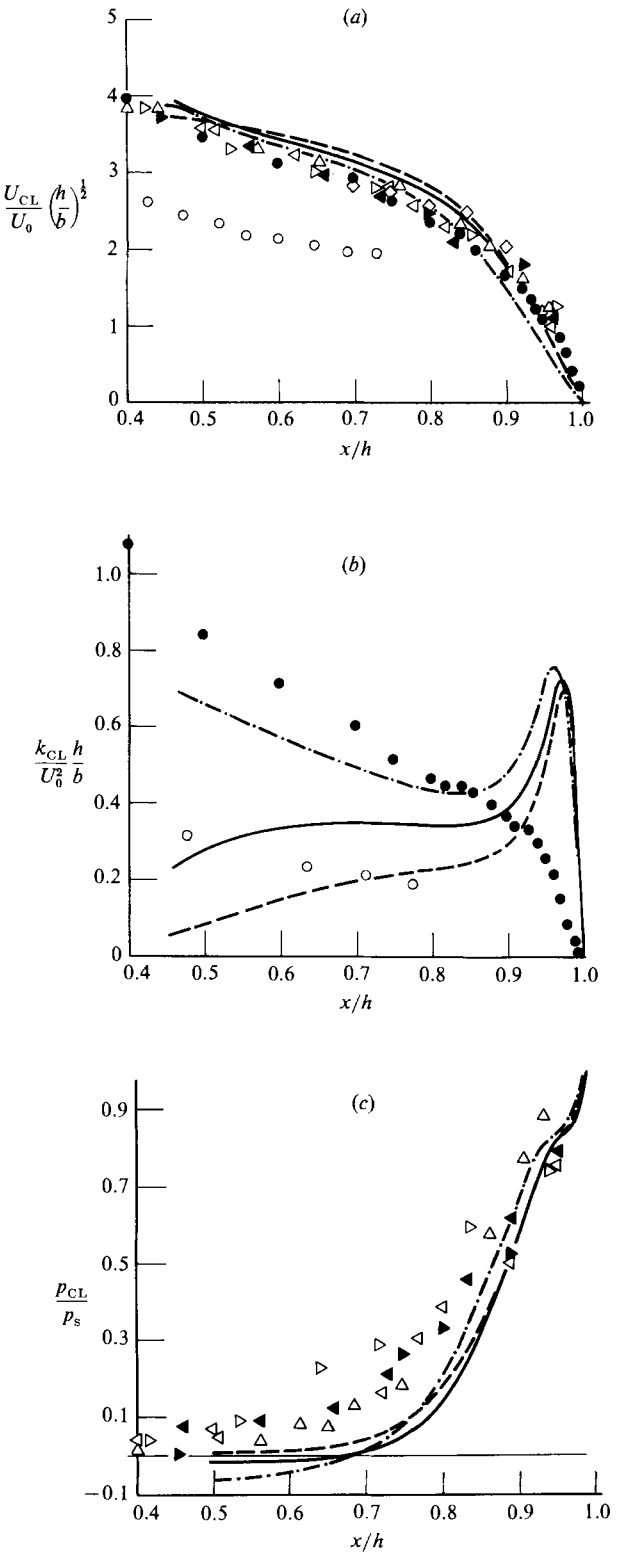

FIGURE 11 (*a*, *b*, *c*). For caption see p. 423.

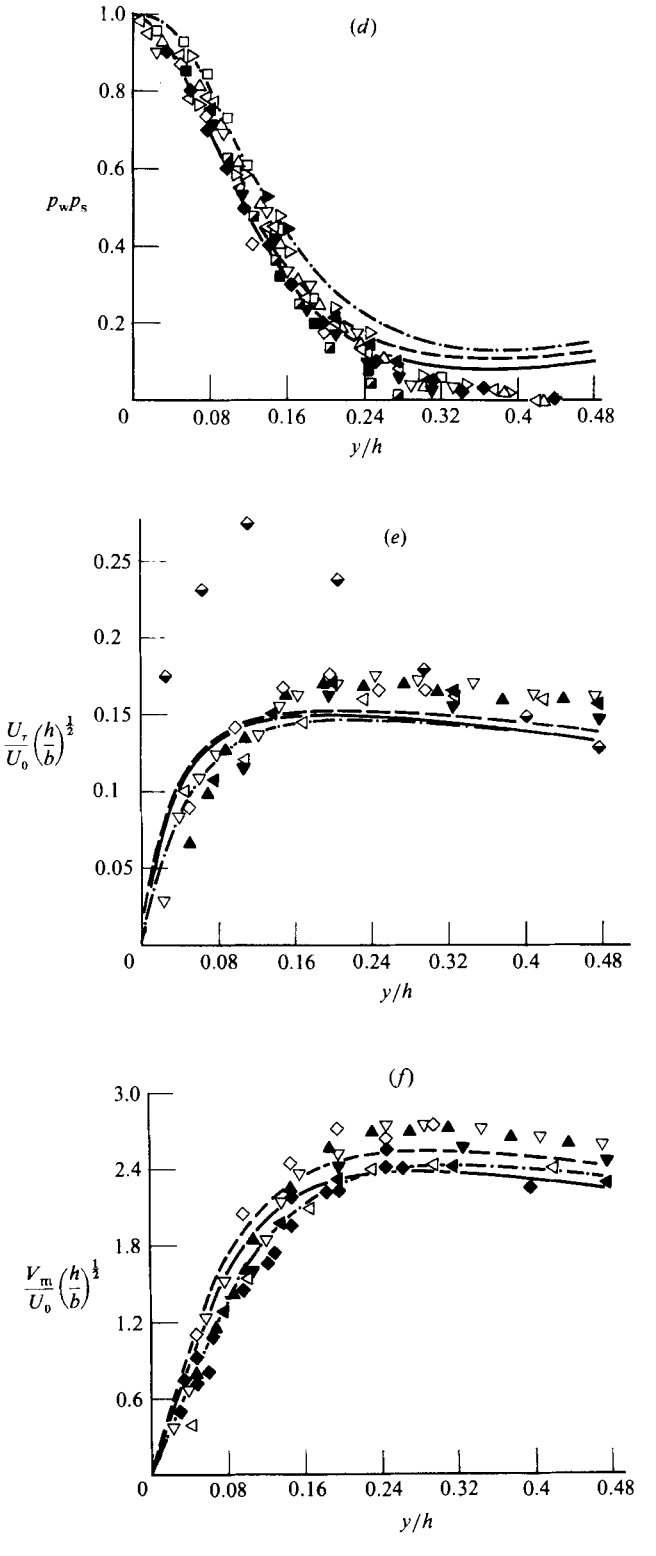

FIGURE 11 (*d*, *e*, *f*). For caption see facing page.

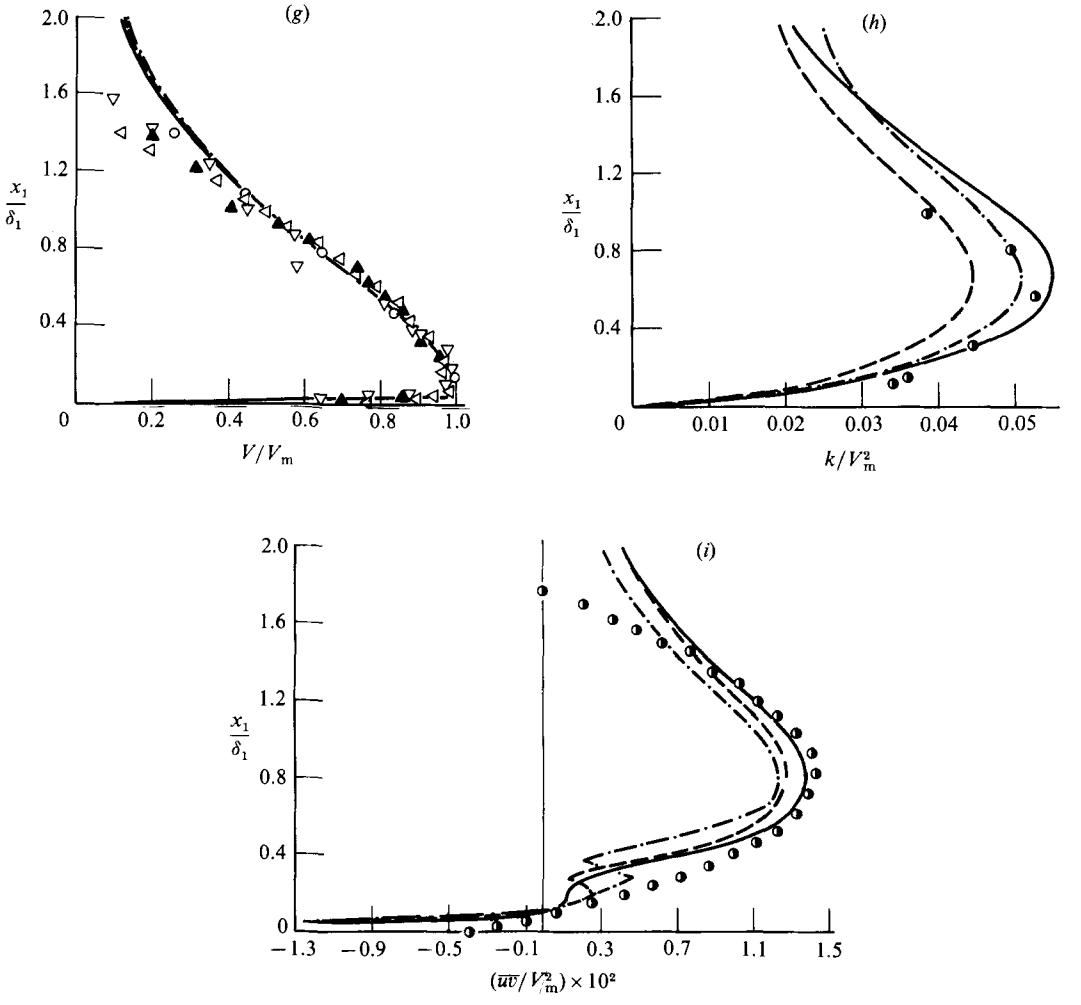

FIGURE 11. Comparison between the numerical solution for the three test cases ($Re_j = 4.2 \times 10^4$, $h/b = 15$ (– – –); 3×10^4, 20 (——); 2.2×10^4, 43 (— — —)) and the experimental data of Beltaos & Rajaratnam at $h/b = 67.5$, $Re_j = 5650$ (△); 66.14, 7100 (▲); 66.14, 5680 (▽); 43.64, 9400 (▼); 43.64, 7100 (◁); 43.64, 5270 (◀); 30.96, 6970 (▷); 14.05, 5270 (▶); Gutmark *et al.* at $Re_j = 3 \times 10^4$, $h/b = 100$ (●); Russell & Hatton at $Re_j = 1.25 \times 10^5$, $h/b = 31$ (○); Schauer & Eustis at $Re_j = 4.3 \times 10^4$, $h/b = 40$ (◇); Baines & Keffer at $Re_j = 7000$, $h/b = 48$ (◈); Kumada & Mabuchi at $Re_j = 7000$–28000, $h/b = 8$–40. (◆); Gardon & Akfirat at $Re_j = 1.1 \times 10^4$, $h/b = 8$ (□); 1.1×10^4, 16 (■); 1.1×10^4, 32 (◪); Tailland & Mathieu plane wall-jet data (◑): (*a*) axial distribution of U_{CL}; (*b*) axial distribution of k_{CL}; (*c*) axial distribution of p_{CL}; (*d*) wall static-pressure profile; (*e*) wall stress distribution; (*f*) variation of V_m with y/h; (*g*) wall jet-velocity profile; (*h*) wall jet k-profile; (*i*) wall jet $\overline{uv}$-profile.

k_{CL} (*b*), V_m (*f*) and τ_w, i.e. ρU_τ^2 (*e*), which are normalized, e.g. by U_0 for U_{CL}, and factorized, e.g. by $(h/b)^{\frac{1}{2}}$ for U_{CL}, in order to compare solutions from differing inlet conditions and h/b ratios respectively. In addition, centreline (*c*) and wall (*d*) static-pressure distributions and wall-jet profiles of V (*g*), k (*h*), and $\overline{uv}$ (*i*) are presented. Owing to the limitations of the data involved, none of the three test cases correspond to the more detailed experiments, e.g. Beltaos & Rajaratnam's (1973) Re_j values were considered too low, the h/b ratio of Gutmark *et al.* was too high, etc. The variation in Re_j over the three cases is selected to facilitate the comparison of

Nusselt-number dependence on Re_j with Gardon & Akfirat's (1965, 1966) data. The hydrodynamic solution is independent of Re_j. Hence any variation in it over the three test cases is a consequence solely of the different h/b ratios.

Excluding Russell & Hatton's (1972) data, which can be accounted for by possible origin shifts and three-dimensional effects, agreement between predictions and experiment for U_{CL} is good. The minor differences between the three test-case distributions and between them and the experimental data are due to 'non-similarity' effects for the lower-h/b cases where undeveloped free jets enter the impingement region. These are highlighted by their k_{CL} distributions where the level of k in the free-jet region reflects the relative developed state of the jet, e.g., for test case 2, $x = 0.45h = 6.75b$ downstream from the nozzle; and for the measurements of Gutmark *et al.* (1978), $x = 0.4h = 40b$. In contrast with the experimental data, all three test-case predictions indicate a sharp rise in k_{CL} beyond $0.8h$ downstream, which results in the enhanced heat-transfer characteristics near the stagnation point. The relative rise in k_{CL} decreases with increasing h/b ratio and its position, i.e. of $k_{CL\max}$, moves away from the stagnation point. Both effects could result in agreement with the data of Gutmark *et al.* for $h/b = 100$, where there appears to be a levelling off of the fall in k_{CL} at $x = 0.82h$. Hence considering Russell & Hatton's data to be spurious, and the good agreement with experiment of the mean-flow variables and heat-transfer characteristics, it must be concluded that no firm evidence exists that contradicts the predictions, at least at levels of h/b greater than 8, Agarwal & Bower (1982) having reported a large overshoot in their predictions of k_{CL} compared with their measurements for their lift jet configuration at $h/b = 2$.

The agreement between predictions and experiment for both the centreline and wall static-pressure measurements is less ambiguous. In the case of p_{CL} the two high-h/b cases correctly indicate the below-ambient pressure in the free-jet region. The predictions show no effect of the wall on the free jet until after $0.7h$ downstream, in agreement with both the U_{CL} and k_{CL} results and experimental observation. This confirms the use of the free-jet inlet conditions at $0.45h$. The discontinuity in the predicted distributions at $0.9h$ may be the result of solving for p rather than p_s, whereas the slight rise in the predicted wall profiles in the outer region, particularly in the case of the highest-h/b case, is due to the approximate side-boundary conditions.

The wall shear-stress predictions are satisfactory close to the stagnation point, while in the outer region they could be improved by employing Ljuboja & Rodi's (1979) model (see figure 10*b*), in agreement with their results for plane wall jets. However, considering that Beltaos & Rajaratnam estimated an uncertainty level of $\pm 6\%$ in their measurements, the predictions from the standard model appear adequate, once Baines & Keffer's (1980) data are discarded. Mean-velocity results in the near-wall flow, as represented by the distribution of V_m and the wall-jet velocity profile in the outer region, also prove to be in good agreement with the experimental data. The wall-jet profiles of k and $\overline{uv}$ compared with Tailland & Mathieu's (1967) experimental data for plane wall jets also indicate adequate agreement, considering the different upstream conditions of the jets. The position of the maximum values in both profiles lie close to each other and to that of the maximum mean-velocity gradient $\partial V/\partial x_1$. The discontinuity in the predicted $\overline{uv}$-profiles is a result of the coarseness of the grid (owing to the use of wall functions), and corresponds to zero $\partial V/\partial x_1$ (with small positive $-\partial U_1/\partial y$).

Figure 12 compares the predictions of stagnation Nusselt number Nu_s for 26 separate test-case solutions with the available experimental data listed in table 2,

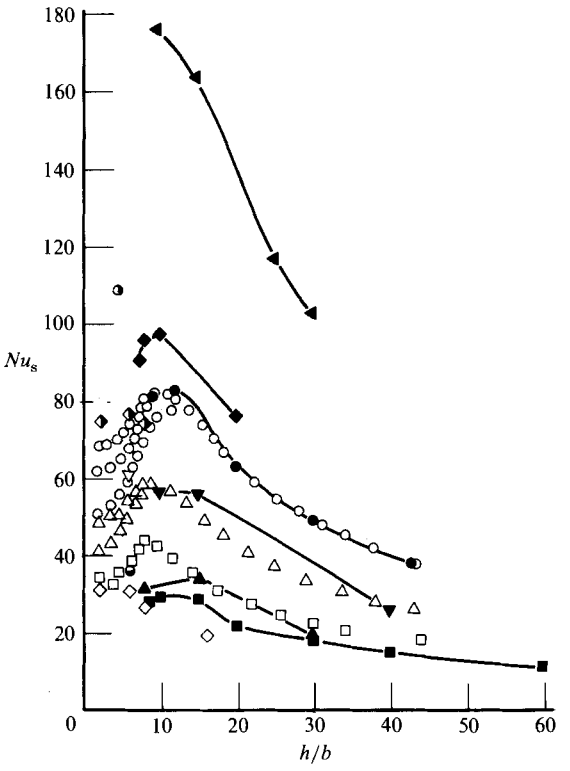

FIGURE 12. Comparison of stagnation-Nusselt-number predictions at $Re_j = 6000$ (-■-); 11000 (-▲-); 14000 (-▼-); 22000 (-●-); 30000 (-◆-); 50000 (-◀-) with the experimental data of Gardon & Akfirat at $Re_j = 5500$ (□); 11000 (△), 22000 (○); Hardisty at $Re_j = 7000$ (◇) and 10000 (◒); Van Heiningen *et al.* at $Re_j = 13700$ (▽); 23300 (◈); 49100 (◑).

which mainly consists of Gardon & Akfirat's measurements. Converged solutions are difficult to achieve for low-h/b cases, i.e. < 8. Accordingly, the confidence in these Nu_s values is reduced, particularly as the jet is not fully turbulent on impingement. However, the correct peak at $h/b = 8$, where k_{CL} is a maximum in a free jet (see figures 6*a*, *e*), is clearly evident in the $Re_j = 22000$ and 30000 cases. Indeed, agreement between predictions and Gardon & Akfirat's data is excellent in this midrange of Re_j (viz the 14000 and 22000 cases), particularly as the 30000 case predictions are in agreement with their overall empirical correlation given by

$$Nu_s = 1.2 Re_j^{0.58} \left(\frac{h}{b}\right)^{-0.62} \pm 5\%, \tag{18}$$

where $14 < h/b < 60$, $2000 < Re_j < 50000$. However, agreement is poor for $Re_j = 50000$, where Nu_s is predicted 30% higher than that given by (18), and for the low Re_j cases considered, though Hardisty's (1977) measurements at $Re_j = 7000$ are in closer agreement. The computational results imply a stronger dependence of Nu_s on Re_j than that of (18), of approximately $Re_j^{0.8}$. However, considerably more computational work is required to confirm this.

The scatter in Gardon & Akfirat's data at low h/b ratios, shown in figure 12, is due to three separate levels of inlet turbulence intensity being present, corresponding to the three nozzle sizes employed. The higher inlet turbulence intensity increases Nu_s below $h/b = 8$, as it reduces the potential-core length, and the secondary peaks which

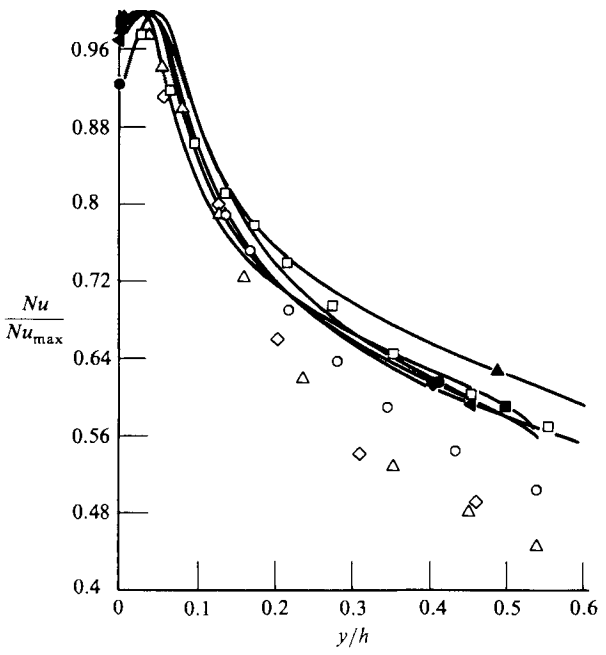

FIGURE 13. Comparison of Nusselt-number wall-profile predictions at $Re_j = 50000$, $h/b = 30$ (-◀-); 42000, 15 (-■-); 30000, 20 (-◆-); 22000, 43 (-●-); 11000, 30 (-▲-) with the experimental data of Gardon & Akfirat at $Re_j = 50000$ (□); 22000 (○); 11000 (△) and $h/b > 8$; Hardisty at $Re_j = 7000$, $h/b = 16$ (◇).

appear in the experimental lateral Nu-profile are correspondingly reduced since they result from a laminar–turbulent transition. These observations agree well with the free-jet k_{CL} predictions and the results of tests undertaken to determine the effect of inlet turbulence level on the free jet, which indicated higher levels of k_{CL} up to $x < 12b$ with little effect beyond this point. Owing to low-Reynolds-number turbulence-modelling difficulties and convergence problems caused by the limitations of the line-by-line solution procedure, these effects are not fully investigated for impinging jet flows.

Figure 13 compares the local Nu wall-profile results for five test cases with Gardon & Akfirat's and Hardisty's measurements. The dependence of profile shape on Re_j obtained by Gardon & Akfirat is not evident in the predicted profiles. A higher profile is found for the lowest-Re_j case, but this appears to be the fault of too low a Nu_s, as is evident from figure 12, being identical to a lower Re_j case at the same h/b ratio. The predicted profiles are in good agreement with Gardon & Akfirat's higher-Re_j measurements. Considering the Re_j independence of all flow properties, including τ_w and V_m, the Nu-predictions appear to be consistent. Therefore further experimental evidence is required before the validity of the heat-flux wall function (14) can be fully assessed.

Overall the predictions have proved satisfactory when compared with the limited experimental data available. In the impingement region the flow is strongly dominated by non-viscous phenomena, and hence the agreement in the case of axial velocity and static pressure is not surprising, being almost independent of the turbulence model employed (see U_{CL}/U_0 in figure 10a). However, the success of the standard k-ϵ model

in predicting the stagnation Nusselt number, the Nu-profile and the wall-jet k- and $\overline{uv}$-profiles must not be underestimated, since it represents a significant modelling achievement when viewed in the light of previous work.

6. Conclusions

The computational results have clearly demonstrated the suitability of both the numerical method and the turbulence models selected in the prediction of free- and impinging-jet flows. Both the laminar free-jet solution and the grid-independence tests for both turbulent-flow solutions have illustrated the accuracy of the numerical procedure in predicting jet flows with reasonably sized meshes ($< 40^2$ nodes). Agreement between predictions and the available experimental data in the literature for the turbulent-flow cases is adequate in almost all cases, with minor differences being satisfactorily accounted for by the correct interpretation of both the predictions and the measurements with respect to inlet and boundary conditions.

The improvement in the prediction of both mean- and turbulent-flow quantities for a developing plane free jet on employing Rodi's (1972) algebraic stress model in place of the standard k-ϵ model has been clearly demonstrated. The spreading rate $\mathrm{d}\delta/\mathrm{d}x$ of the jet has been shown to be a constant and equal to 0.1, in agreement with the bulk of the experimental data. In addition the difficulties associated with interpreting both static pressure and turbulence-energy dissipation-rate measurements have been highlighted.

The limitatons of modified k-ϵ turbulence models have been illustrated by the Nusselt-number predictions, satisfactory results being obtained exclusively by the standard model, whose applicability to recirculating flows has once again been demonstrated. The lack of universality of any one model illustrates the theoretical limitations inherent in the derivation of all two-equation models and emphasizes the need for the development of adequate alternative approaches, e.g. Reynolds-stress equation modelling, subgridscale modelling, spectral methods.

The enhanced heat-transfer characteristics near the stagnation point of an impinging jet have been verified, and shown to be a direct result of the high turbulence kinetic-energy levels present. However, the true level of $k_{\mathrm{CL\,max}}$ reached is still debatable owing to insufficient experimental verification. The resulting local Nusselt-number profile along the plate has been shown to be Reynolds-number independent, which is contrary to Gardon & Akfirat's (1965, 1966) measurements, but is consistent with the hydrodynamic predictions. Finally, the resulting developing wall jet from a plane impinging jet flow has been shown to be identical with the standard plane wall-jet configuration.

The authors are indebted to the authorities of University College Dublin and the Minister of Education for the support which made this work possible.

REFERENCES

AGARWAL, R. K. & BOWER, W. W. 1982 *AIAA J.* **20**, 577–584.

ALCARAZ, E., CHARNAY, G. & MATHIEU, J. 1977 *Phys. Fluids* **20**, 203–210.

ANDRADE, E. N. 1939 *Proc. Phys. Soc. Lond.* **51**, 784–793.

ANTONIA, R. A., SATYAPRAKASH, B. R. & HUSSAIN, A. K. M. F. 1980 *Phys. Fluids* **23**, 695–700.

BAINES, W. D. & KEFFER, J. F. 1980 In *Drying '80* (ed. A. Mujumdar), vol. 1, pp. 376–382.

BELTAOS, W. D. & RAJARATNAM, N. 1973 *J. Hydraul. Res.* **11**, 29–59.

BICKLEY, W. 1939 *Phil. Mag.* (7) **23**, 727–731.

BOWER, W. W. & KOTANSKY, D. R. 1976 *AIAA Paper* 76–621.

BOWER, W. W., KOTANSKY, D. R. & HOFFMAN, G. H. 1977 In *Proc. Symp. Turbulent Shear Flows*, pp. 3.1–3.8.

BRADBURY, L. J. S. 1965 *J. Fluid Mech.* **23**, 31–64.

BRADSHAW, P. 1977 *J. Fluid Mech.* **80**, 795–797.

CROW, S. C. 1968 *J. Fluid Mech.* **33**, 1–20.

FORTHMANN, E. 1934 *Ing. Arch.* **5**, 42–54.

GARDON, R. & AKFIRAT, J. C. 1965 *Intl J. Heat Mass Transfer* **8**, 1261–1272.

GARDON, R. & AKFIRAT, J. C. 1966 *Trans. ASME* C: *J. Heat Transfer* **88**, 101–108.

GUTMARK, E., WOLFSHTEIN, M. & WYGNANSKI, I. 1978 *J. Fluid Mech.* **88**, 737–756.

GUTMARK, E. & WYGNANSKI, I. 1976 *J. Fluid Mech.* **73**, 465–495.

HANJALIC, K. & LAUNDER, B. E. 1972 *J. Fluid Mech.* **52**, 609–638.

HARDISTY, H. 1977 *J. Oil Col. Assn* **60**, 479–487.

HESKESTAD, G. 1965 *Trans. ASME* E: *J. Appl. Mech.* **32**, 721–7324.

HUSSAIN, A. K. M. F. & CLARK, A. R. 1977 *Phys. Fluids* **20**, 1416–1426.

JAYATILLEKE, C. L. V. 1969 *Prog. Heat Mass Transfer* **1**, 193–329.

JONES, W. P. & LAUNDER, B. E. 1972 *Intl J. Heat Mass Transfer* **15**, 301–314.

JONES, W. P. & LAUNDER, B. E. 1973 *Intl J. Heat Mass Transfer* **16**, 1119–1130.

KOLMOGOROV, A. N. 1942 *Izv. Akad. Nauk SSSR, Ser. Phys.* **6**, 56–58.

KOTSOVINOS, N. E. 1976 *J. Fluid Mech.* **77**, 305–311.

KUMADA, M. & MABUCHI, I. 1970 *Bull. JSME* **13**, 77–85.

LAUNDER, B. E. 1975 *J. Fluid Mech.* **67**, 569–581.

LAUNDER, B. E. & MORSE, A. 1977 In *Proc. Symp. Turbulent Shear Flows*, pp. 421–430.

LAUNDER, B. E., MORSE, A., RODI, W. & SPALDING, D. B. 1972 In *Proc. Conf. Free Turbulent Shear Flows*, p. 361; *NASA SP* 321.

LAUNDER, B. E., REECE, G. J. & RODI, W. 1975 *J. Fluid Mech.* **68**, 537–566.

LAUNDER, B. E. & SPALDING, D. B. 1974 *Comp. Meth. Appl. Mech. Engng* **3**, 269–289.

LJUBOJA, M. & RODI, W. 1979 In *Proc. Symp. Turbulent Boundary Layers*: *Forced, Incompressible Non-Reacting* (ed. H. E. Weber), pp. 131–138.

LOONEY, M. K. 1982 Ph.D. thesis, Dept Chem. Engng, University College Dublin.

LOONEY, M. K. & WALSH, J. J. 1982 In *Proc. Symp. on Refined Modelling of Flows*, vol. 1, pp. 261–271.

MATHIEU, J. 1971 *Von Kármán Inst., Lect. Ser.* 36.

MIH, W. C. & HOOPES, J. A. 1972 *J. Hydraul. Div. ASCE* **00** (HY7), 1275–1294.

MILLER, D. R. & COMINGS, E. W. 1957 *J. Fluid Mech.* **3**, 1–16.

NEWMAN, B. G. 1967 In *Fluid Mechanics of Internal Flow* (ed. G. Sovran), pp. 170–209. Elsevier.

PATANKAR, S. V. & SPALDING, D. B. 1967 *Heat and Mass Transfer in Boundary Layers.* Morgan-Grampion.

PATANKAR, S. V. & SPALDING, D. B. 1972 *Intl J. Heat Mass Transfer* **15**, 1787–1806.

PATEL, R. P. 1970 Ph.D. thesis, McGill University, Montreal.

PRANDTL, L. 1945 *Nachr. Akad. Wiss. Gött.* pp. 6–19.

PUN, W. M. & SPALDING, D. B. 1976 *Imp. Coll. Lond. Mech. Engng Dept Rep.* HTS/76/2 (amended August 1977).

ROBINS, A. G. 1973 Ph.D. thesis, University of London.

RODI, W. 1972 Ph.D. thesis, University of London.

RODI, W. 1975 In *Studies in Convection* (ed. B. E. Launder), pp. 79–165.

RODI, W. 1980 In *Prediction Methods for Turbulent Flows* (ed. W. Kollman), pp. 259–349. Von Kármán Inst.

RODI, W. & SPALDING, D. B. 1970 *Wärme- und-Stoffübertragung* **3**, 85–95.

ROTTA, J. 1969 *Aerodyn. Versuchsanstalt Gött. Rep.* 69 A14.

RUSSELL, P. J. & HATTON, A. P. 1972 *Proc. Inst. Mech. Engrs* **186**, 635–644.

SCHAUER, J. J. & EUSTIS, R. H. 1963 *Stanford Univ. Tech. Rep.* 3.

SCHLICHTING, H. 1933 *Z. angew. Math. Mech.* **13**, 260–263.

TAILLAND, A. & MATHIEU, J. 1967 *J. Méc.* **6**, 103.

VAN DER HEGGE ZIJNEN, B. G. 1958 *Appl. Sci. Res.* A **7**, 256–313.

VAN HEININGEN, A. R. P., MUJUMDAR, A. S. & DOUGLAS, W. J. M. 1977 In *Proc. Symp. Turbulent Shear Flows*, pp. 3.9–3.15.

WOLFSHTEIN, M. 1967 Ph.D. thesis, Imperial College London.

WOLFSHTEIN, M. 1969 *Imp. Coll. Lond., Mech. Engng Dept Rep.* EF/TN/A/17.